The Astrophysical Journal, 962:96 (21pp), 2024 February 10 https://doi.org/10.3847/1538-4357/ad0fd8

High-spectral-resolution Observations of the Optical Filamentary Nebula Surrounding NGC 1275

Benjamin Vigneron[1,19], Julie Hlavacek-Larrondo[1,2], Carter Lee Rhea[1,2], Marie-Lou Gendron-Marsolais[3], Jeremy Lim[4], Jake Reinheimer[5], Yuan Li[5], Laurent Drissen[2,6,7,8], Greg L. Bryan[9,10], Megan Donahue[11], Alastair Edge[12], Andrew Fabian[13], Stephen Hamer[13], Thomas Martin[2,6], Michael McDonald[14], Brian McNamara[15], Annabelle Richard-Lafferrière[16], Laurie Rousseau-Nepton[8], G. Mark Voit[11], Tracy Webb[17], and Norbert Werner[18]
[1] Département de Physique, Université de Montréal, Succ. Centre-Ville, Montréal, Québec H3C 3J7, Canada; benjamin.vigneron@umontreal.ca
[2] Centre de recherche en astrophysique du Québec (CRAQ), Canada
[3] Instituto de Astrofísica de Andalucía, IAA-CSIC, Apartado 3004, E-18080 Granada, Spain
[4] Department of Physics, The University of Hong Kong, Pokfulam Road, Hong Kong
[5] Department of Physics, University of North Texas, Denton, TX 76203, USA
[6] Département de physique, de génie physique et d'optique, Université Laval, Québec G1V 0A6, Canada
[7] Department of Physics and Astronomy, University of Hawai'i at Hilo, Hilo, HI 96720, USA
[8] Canada–France–Hawaii Telescope, 65-1238 Mamalahoa Hwy, Kamuela, HI 96743, USA
[9] Department of Astronomy, Columbia University, 550 West 120th Street, New York, NY 10027, USA
[10] Center for Computational Astrophysics, Flatiron Institute, 162 5th Avenue, New York, NY 10010, USA
[11] Department of Physics and Astronomy, Michigan State University, East Lansing, MI 48824, USA
[12] Department of Physics, Durham University, South Road, Durham DH1 3LE, UK
[13] Institute of Astronomy, University of Cambridge, Madingley Road, Cambridge CB3 0HA, UK
[14] Kavli Institute for Astrophysics and Space Research, MIT, Cambridge, MA 02139, USA
[15] Department of Physics and Astronomy, University of Waterloo, 200 University Avenue West, Waterloo, ON N2L 3G1, Canada
[16] Institute of Astronomy, University of Cambridge, Madingley Road, Cambridge CB1 0HA, UK
[17] Department of Physics, McGill Space Institute, McGill University, 3600 rue University, Montreal H3A 2T8, Canada
[18] Department of Theoretical Physics and Astrophysics, Faculty of Science, Masaryk University, Brno, Czech Republic
Received 2023 February 8; revised 2023 November 8; accepted 2023 November 24; published 2024 February 9

Abstract

We present new high-spectral-resolution observations ($R = \lambda/\Delta\lambda = 7000$) of the filamentary nebula surrounding NGC 1275, the central galaxy of the Perseus cluster. These observations have been obtained with SITELLE, an imaging Fourier transform spectrometer installed on the Canada–France–Hawai Telescope with a field of view of $11' \times 11'$, encapsulating the entire filamentary structure of ionized gas despite its large size of 80 kpc × 50 kpc. Here, we present renewed fluxes, velocities, and velocity dispersion maps that show in great detail the kinematics of the optical nebula at [S II] λ6716, [S II] λ6731, [N II] λ6584, Hα (6563 Å), and [N II] λ6548. These maps reveal the existence of a bright flattened disk-shaped structure in the core extending to $r \sim 10$ kpc and dominated by a chaotic velocity field. This structure is located in the wake of X-ray cavities and characterized by a high mean velocity dispersion of 134 km s^{-1}. The disk-shaped structure is surrounded by an extended array of filaments spread out to $r \sim 50$ kpc that are 10 times fainter in flux, remarkably quiescent, and have a uniform mean velocity dispersion of 44 km s^{-1}. This stability is puzzling given that the cluster core exhibits several energetic phenomena. Based on these results, we argue that there are two mechanisms that form multiphase gas in clusters of galaxies: a first triggered in the wake of X-ray cavities leading to more turbulent multiphase gas and a second, distinct mechanism, that is gentle and leads to large-scale multiphase gas spreading throughout the core.

Unified Astronomy Thesaurus concepts: AGN host galaxies (2017); Active galaxies (17); Brightest cluster galaxies (181); Filamentary nebulae (535); Perseus Cluster (1214)

1. Introduction

Clusters of galaxies are extended structures hosting several hundred to thousands of gravitationally bound galaxies (e.g., Bahcall 1977; Abell et al. 1989). They are mostly composed of dark matter while galaxies only represent a very small fraction of the cluster's mass (e.g., Sand et al. 2004; Voigt & Fabian 2006). There is also a third component made of hot X-ray emitting gas at temperatures of $\sim 10^7$–10^8 K that fills the space between the galaxies and is known as the intracluster medium (ICM; e.g., Cavaliere et al. 1971; Gursky et al. 1971; Hitomi Collaboration et al. 2016).

This ICM accounts for a substantial fraction of the mass of a cluster (∼13%) and often leads clusters to being classified into two distinct categories depending on their X-ray emission profiles: cool-core clusters with a strongly peaked X-ray emission profile and non–cool-core clusters with a more diffuse and uniform X-ray emission profile (Million & Allen 2009, Hudson et al. 2010). The central dominant galaxy located in the core, known as the brightest cluster galaxy (BCG), often exhibits extended filamentary nebulae of optical ionized gas in the case of cool-core clusters (Crawford et al. 1999, McDonald et al. 2010). These filaments are composed of multiphase gas that have high Hα luminosities (e.g., Conselice et al. 2001), and are often cospatial with cold gas (e.g., Salomé et al. 2006) as well as soft X-ray gas. The most extended filaments can be

[19] Corresponding author.

mostly devoid of star formation, which excludes photoionization as a primary ionization mechanism (e.g., Kent & Sargent 1979).

A promising explanation for the formation of the filamentary nebulae surrounding BCGs resides in the precipitation limit hypothesis (e.g., Gaspari et al. 2012, 2013, 2015, Voit & Donahue 2015; Voit et al. 2015, 2017, Li et al. 2015). Here, the constant cooling by emission of the ICM in cool-core clusters should imply high star formation rates in the cores of clusters. However, since there is limited evidence of correspondingly extremely high star formation inside these galaxies, a mechanism is necessary to stop the gas from cooling and falling in the potential well (e.g., Crawford et al. 1999). In clusters of galaxies, the heating mechanism is thought to be orchestrated by the supermassive black hole (SMBH) residing in the BCG. This mechanism can be seen in action in radio bubbles generated by the central black hole, which carve out large X-ray cavities in the ICM, entailing shocks, turbulence, and mixing (e.g., Graham et al. 2008; Zhuravleva et al. 2014; Randall et al. 2015). This phenomenon will in turn bring enough energy to limit the cooling of the ambient gas and therefore star formation in the galaxy (Crawford et al. 1999, Best et al. 2007; Voit et al. 2008). However, the mechanisms explaining how the active galactic nucleus (AGN) energy reheats the ICM remains a matter of debate.

The precipitation limit hypothesis proposes that the heating process associated with the activity of the AGN sets in motion flows, which in turn encourage the hot surrounding medium to condense at higher altitudes. Hence, the adiabatic uplift of material through radio bubbles promotes condensation by reducing the ratio of the cooling time to freefall time in some locations. This cycle is analogous to precipitation on Earth, where raindrops form by the uplifting of gas higher in the atmosphere. Moreover, simulations show that the rain of cold gas toward the center of the galaxy will initially feed the central black hole, and therefore the power of the flows that it produces, enabling a self-regulated feedback loop (e.g., Voit et al. 2017). This energy from the black hole will, in turn, heat the ambient medium and increase the ratio of the cooling time to the freefall time so that the precipitation will cease. The filamentary nebulae surrounding BCGs have been interpreted as a tell-tale sign of this process and could therefore offer the possibility to study this hypothesis.

Here, we target the filamentary nebula that surrounds NGC 1275, the BCG located at the center of the Perseus cluster of galaxies. NGC 1275 has been studied extensively at all wavelengths (see Forman et al. 1972; Fabian et al. 2011; Salomé et al. 2011; Lim et al. 2012; Nagai et al. 2019). The cluster hosts several X-ray cavities that originate from multiple generations of radio jets emitted from the AGN of NGC 1275 (Boehringer et al. 1993; Fabian et al. 2000, 2011; Gendron-Marsolais et al. 2018). These jets carve the neighboring ICM, creating buoyantly rising radio-emitting bubbles.

NGC 1275 also displays one of the largest filamentary nebulae known, with a size of about 80 kpc × 50 kpc (e.g., McNamara et al. 1996; Conselice et al. 2001; Hamer et al. 2016). Combined with the proximity of the Perseus cluster, this makes NGC 1275 a target of choice for our understanding of the formation and ionization mechanisms of filamentary nebulae in clusters.

The first observations of the filamentary nebula surrounding NGC 1275 by Minkowski (1957), Lynds (1970), and Rubin et al. (1977) unveiled a high-velocity (HV) feature ($\sim$8200 km s^{-1}) associated with a forefront spiral galaxy falling onto NGC 1275 (Yu et al. 2015), and a low-velocity (LV) structure ($\sim$5200 km s^{-1}) linked to NGC 1275. Hubble Space Telescope observations of the LV structure then revealed the filamentary appearance of the ionized gas (Fabian et al. 2008), whereas soft X-ray counterparts were discovered for certain bright filaments with the Chandra X-Ray Observatory (Fabian et al. 2003). Moreover, cold molecular gas has been associated with the emission of the filamentary nebula of NGC 1275 (Salomé et al. 2006, Ho et al. 2009; Salomé et al. 2011; Mittal et al. 2012), and also linked to a disk of emission near the galaxy (Lim et al. 2008).

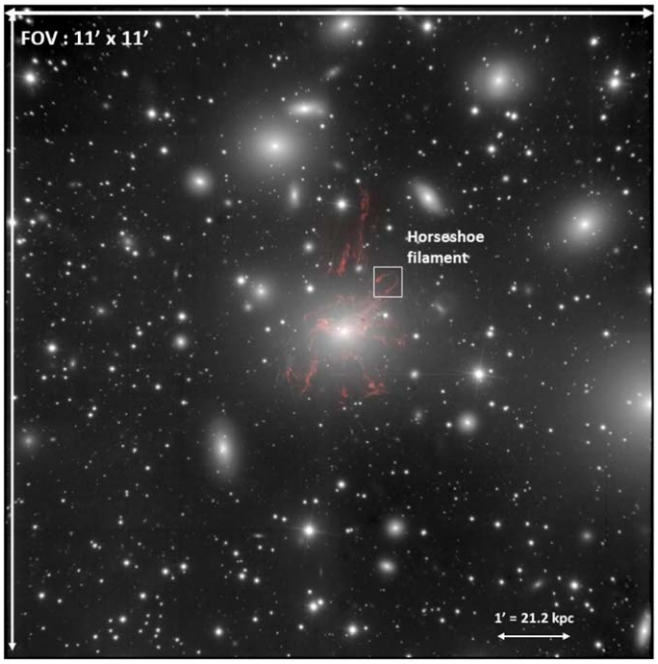

Figure 1. The complete field of view (11′×11′) of the SITELLE observations of NGC 1275 with the full-band SN3 filter (648–685 nm) at high spectral resolution ($R = 7000$). Here, we show the integrated flux images in gray scale with the brightest Hα filaments in red. The white square denotes the Horseshoe filament.

Nevertheless, the first detailed observations of the nebula were performed by Conselice et al. (2001) with high-resolution imaging and integral field and long-slit spectroscopy (performed at the Wisconsin–Indiana–Yale–NOIRLab (WIYN) Observatory and Kitt Peak National Observatory, respectively). These observations produced the first velocity map of the central $\sim$45″ ($\sim$16.5 kpc) of the nebula. Observations from the Gemini Multi-Object Spectrograph from six slits carefully positioned along certain filaments showed evidence of outflowing gas and flow patterns (Hatch et al. 2006). In 2018, the filamentary nebula was then imaged for the first time with the Spectromètre Imageur à Transformée de Fourier pour l'Etude en Long et en Large de raies d'Emission (SITELLE), an imaging Fourier transform spectrometer (Drissen et al. 2019) installed at the Canada–France–Hawaii Telescope (CFHT) that has an extremely large field of view (11′ × 11′) capable of imaging the nebula in its entirety (see Figure 1). Gendron-Marsolais et al. (2018) showed that the velocity structure of the filaments appears to be generally devoid of specific trends or rotation.

In this paper, we present new high-spectral-resolution observations of the filamentary nebula surrounding NGC 1275 obtained with SITELLE. The first SITELLE observations presented in

Gendron-Marsolais et al. (2018) revealed the kinematics of the ionized nebula, but suffered from poor spectral resolution ($R = 1800$) that could not spectroscopically resolve the filaments beyond a projected radius of $r \gtrsim 10$ kpc centered on the AGN.

Here, the high-spectral-resolution nature of the data at $R = 7000$ allows us to deepen the scope of the study by performing a detailed analysis of the kinematics of the nebula, in particular the velocity dispersion of the gas. The analysis of the data revealed a central structure displaying a higher mean flux and velocity dispersion than the rest of the outer filaments. This disk-shaped structure seems spatially correlated with a similar structure of cold molecular gas, which will be detailed in later sections. This result appears relevant when considering the clear kinematic correlations between the ionized and molecular gas in the central region, as well as possibly far-infrared (FIR) [C II] emission lines of the gas surrounding NGC 1275 as observed with Herschel by Mittal et al. (2012).

In Section 2, we present the new SITELLE observations and the various procedures used during the data analysis. In Section 3 we present and discuss our results. Finally, a summary of our conclusions will be presented in Section 4.

To compare our results to those of Gendron-Marsolais et al. (2018) and the Hitomi Collaboration et al. (2018) directly, we also adopt for NGC 1275 a redshift of $z = 0.017284$, which implies an angular scale of 21.2 kpc arcmin^{-1}. This z also corresponds to a luminosity distance of 75.5 Mpc, assuming $H_0 = 69.6$ km s^{-1}Mpc^{-1}, $\Omega_M = 0.286$, and $\Omega_{\rm vac} = 0.714$.

2. Data Analysis

2.1. Observations with SITELLE

The filamentary nebula surrounding NGC 1275 was observed in 2020 February with SITELLE during queued service observation 20AD99 by PIs Hlavacek–Larrondo and Rhea. SITELLE is a Fourier transform imaging spectrometer with an incredibly large field of view of 11′ by 11′ and equipped with two E2V detectors of 2048×2064 pixels, resulting in a spatial resolution of $0\farcs321 \times 0\farcs321$. SITELLE was used with the SN3 filter for 4 hr (1710 exposures of 8.42 s) including overheads, necessary to obtain a high-spectral resolution of $R = 7000$. This filter covers wavelengths from 648 to 685 nm. These observations were centered on NGC 1275 with R.A. = 03:19:48.16 and decl. = +41:30:42.1. Five emission lines are covered with the SN3 filter, namely [S II] λ6716, [S II] λ6731, [N II] λ6584, Hα (6563 Å), and [N II] λ6548. The oxygen emission lines [O I] λ6300 and [O I] λ6363 could not be observed in such a configuration since they fall just outside of the spectral range of the SN3 filter (648–685 nm). The data reduction of SITELLE is performed at CFHT through a dedicated pipeline: Outil de Réduction Binoculaire pour SITELLE (ORBS). We summarize the reduction process here. The electronic bias and the flat-field curvature of the interferometric images are first corrected. Images are then aligned to solve potential guiding errors. Cosmic rays are detected through an algorithm comparing successive images to determine if any abnormal flux increase can be observed for a given pixel. These detections are corrected by an estimation of the given Gaussian flux of nearby pixels. Atmospheric variations are also taken into account and corrected through a transmission function taken during the data acquisition. The reduction pipeline then produces the Fourier transform of all the interferograms contained within the data cube, which are then phase corrected. Finally, wavelength and flux calibrations are performed to record the high-spectral resolution observations adequately (Drissen et al. 2019).

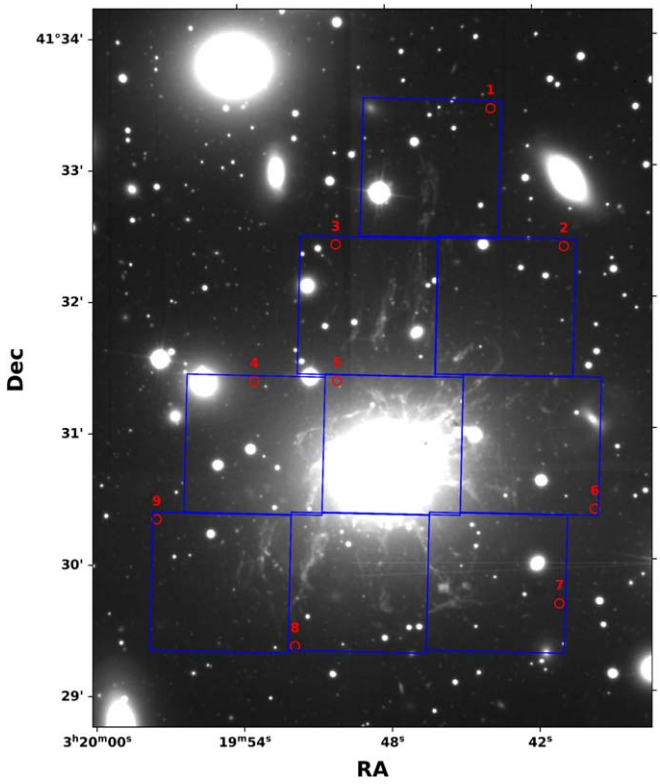

Figure 2. Mosaic map used during the analysis to tackle the background variability issue. The blue squares represent the regions whose spectra are fitted by LUCI, while the red circles denote the regions whose emission was used for background subtraction. The gray scale background of the figure is a deep image of the filaments surrounding NGC 1275 produced with LUCI.

2.2. Background Subtraction

After a careful evaluation of the high-spectral resolution data obtained with SITELLE, it became clear that an important variability of the background emission across the field of view is present in the spectra (see Appendix A). This background emission is mainly produced by galaxies present near the filamentary nebula as well as diffuse emission from other structures in the field of view. Background subtraction is therefore needed to disentangle this unwanted emission properly from the filament emission lines; however, this procedure is not taken into account in the reduction pipeline. This step must therefore be performed during the fitting procedure. The background variability affects mainly the analysis of the [S II] λ6717 and [S II] λ6731 emission lines, which are much fainter than the other optical lines. To tackle this issue, we decided to divide the entire filamentary nebula into nine regions as illustrated in Figure 2. For each of these nine regions, we attributed a specific sky zone devoid of targeted emission lines and located within the boundaries of that region. The red circles shown in Figure 2 illustrate these nine sky zones. The sky zones are then used during the fitting procedure to perform background subtraction for each dedicated region. Once all the regions have been fitted properly (see following sections), we then create a mosaic of the flux, velocity, and dispersion maps for the complete filamentary nebula. This procedure allows us to counter the background

variability by considering several background regions instead of one to increase the reliability of our results. The development of a dedicated methodology to tackle background variability in detail for SITELLE data will be part of a future paper.

2.3. Weighted Voronoi Tessellation

During a preliminary analysis of the high-spectral-resolution data of NGC 1275, we noticed that the signal-to-noise ratio (S/N) of the filamentary nebula was relatively low compared to what was expected from the SITELLE Exposure Time Calculator. Poor weather conditions during the data acquisition are considered to be the main cause of a lower S/N (see Appendix B for an example of the S/N map).

Thus, to tackle this issue, we decided to implement a weighted Voronoi tessellation (WVT) algorithm as a feature of the `LUCI` software using the tool Xtra-Astonomy (https://github.com/XtraAstronomy/AstronomyTools; Rhea et al. 2020b). This procedure creates bins of pixels whose S/Ns are defined by a threshold chosen by the user. Therefore, regions with strong emission will be contained within smaller bins, while noisier regions will be grouped into larger bins compared to regions of interest such as filaments. This also leads to the presence of bins containing a single pixel where the S/N is already high.

More specifically, we started by making an S/N map of the filamentary nebula by only considering the Hα emission line and [N II] emission line doublet. The S/N map is produced by determining the ratio of the maximum value of the emission lines by the standard deviation of the spectra in a wave band devoid of emission lines. The pixels are then aggregated to create the bins and reach the S/N threshold established. In our case, we decided to fix the S/N level to 30, which is close to the estimated value of S/N = 35 for most of the filaments that would have been obtained in ideal observing conditions with SITELLE. From there, we established the number of bins defined by the algorithm and created numpy files of pixels coordinates for each to be used later in the spectral fitting procedure. The function `wvt_fit_region` of `LUCI` can be called to produce the fitting of a specific region of the image, which will be run through the weighted Voronoi algorithm first.

One example of the WVT procedure can be seen in Figure 3 where the algorithm has been applied to the horseshoe filament shown in Figure 1. It illustrates that the WVT code manages to improve the flux detection of the base of the horseshoe compared to the background emission. However, the flux of the filament's upper region remains too low to be properly detected and accounted for in the resulting flux map. We therefore applied a flux threshold of 2×10^{-17} erg s^{-1} cm^{-2} after the fitting to our final maps to eliminate unwanted bins of noisy data displaying a higher flux properly. A similar flux threshold was also applied in the analysis of low-spectral-resolution observations with SITELLE by Gendron-Marsolais et al. (2018).

2.4. Masking Procedure

To help the fitting process, we decided to implement a masking procedure designed to keep as much information about the filamentary nebula as necessary. To implement this mask, we used the observational data presented by Conselice et al. (2001) and produced by the WIYN 3.5 m telescope. These deep observations showed the filamentary nebula surrounding NGC 1275 with higher S/Ns; therefore, by using these observations as a basis for our masking procedure, we can retain the necessary information for our fitting results.

The procedure used to develop this mask was implemented as follows: first, a threshold S/N value of 10 in the Conselice et al. (2001) WIYN data was chosen in order to retain as much information regarding the filaments as possible without keeping too many background pixels in the resulting image.

Second, for the mask to be used in conjunction with the `LUCI` software, some groundwork was needed to match the size and position of the mask perfectly with our SITELLE data according to the WCS coordinates of the latter. Indeed, the WIYN observations did not have the same astrometry as our data, meaning that they were not properly aligned. Moreover, the number of pixels in both observations are not the same, which required specific care to handle their interpolation.

To solve this issue, we determined the number of pixels needed to cover the entirety of the SITELLE field of view by considering the pixel dimensions of both the SITELLE and WIYN instruments. Then, by knowing the position of the central pixel of the SITELLE data cube using the decl. and R. A., we were able to determine the corresponding pixel on the mask. Thus, by knowing the number of pixels needed as well as the central pixel we used the function `Cutout2D` from the `astropy.nddata` package to extend our mask to fit the SITELLE field of view. We then interpolated the mask onto the specific dimensions of the SITELLE observations using the function `interp2d` from the `scipy.interpolate` package, therefore creating a fitted mask without losing its nature despite having different dimensions originally (see Figure 4).

Finally, to align the mask with the SITELLE data properly, we used the WCS coordinates given within the SITELLE data cube to determine the positions of 11 stars, which then acted as anchor points for the `estimate_transform` and `apply_transform` functions of the `astroalign` package. By determining the positions of these stars within the newly produced mask, we matched them to their positions in the SITELLE data and allowed the images to overlap.

2.5. Emission Line Fitting Procedure

After obtaining our mask to the SITELLE data cube, we were able to proceed to the emission line fitting part of the analysis. The recent software `LUCI` was used to perform the fit (Rhea et al. 2020a, 2020b, 2021a, 2021b) according to our mosaic structure detailed previously. Since `LUCI` is a novel analysis software, a summary of `LUCI` capabilities is described here but we invite the user to see https://crhea93.github.io/LUCI/index.html for more details (Rhea et al. 2021a).

First, the spectra found in the data cube are normalized according to the highest amplitude and a shift in wavelength is applied to center the velocities properly between -500 and 500 km s^{-1}. This constraint is necessary for the following procedure that uses machine learning since it allows better prior estimates for the fitting algorithm. This velocity range was chosen after a visual inspection of the data and considering the previous work by Gendron-Marsolais et al. (2018). These boundaries were given as training parameters for the neural network to predict the velocity shifts of the emission lines. To fit a spectrum efficiently, the velocity and broadening prior information need to be precise for the minimization algorithm at the heart of the emission lines fitting and thus to accelerate

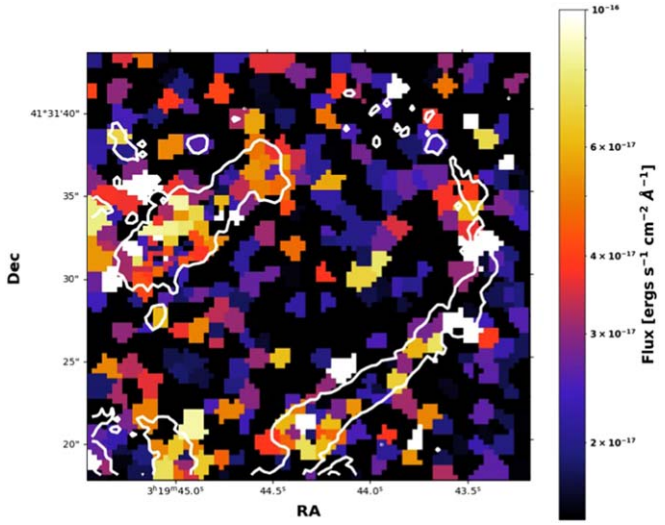

Figure 3. Example of a WVT performed by LUCI to produce the resulting Hα flux map after fitting the spectra of the horseshoe filament, whose general contours, taken from the mask displayed in Figure 4, are superimposed on the figure as white contours. In this case, we chose an S/N value equal to 30.

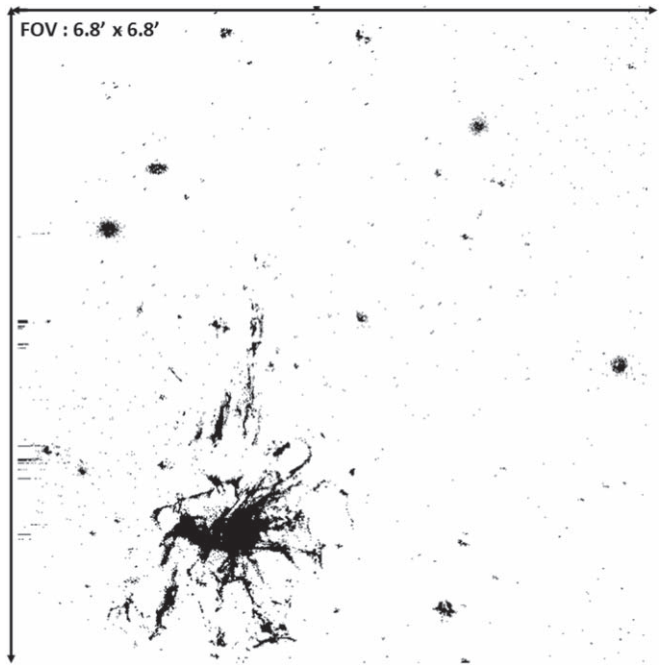

Figure 4. Applied mask to the SITELLE data of NGC 1275. White pixels are masked while black pixels are unmasked. The data used to produce this mask come from the high-spatial-resolution images taken by Conselice et al. (2001) with the WIYN telescope. Note that the field of view is smaller than the field of view of the SITELLE observations, but covers the filaments.

the whole procedure (Zeidler et al. 2019, Bittner et al. 2019). Therefore, a machine-learning technique based on a convolutional neural network (CNN) is used to determine these priors properly.

From there, the values obtained through the CNN are the line position and broadening. The amplitude, however, is obtained from the height of the shifted emission line. With these three values, the line can be effectively fitted by LUCI with the `scipy.optimize.minimize` function from the `scipy` package. This function uses the sequential least squares programming (SLSQP) optimization algorithm. Since SITELLE's instrumental spectra

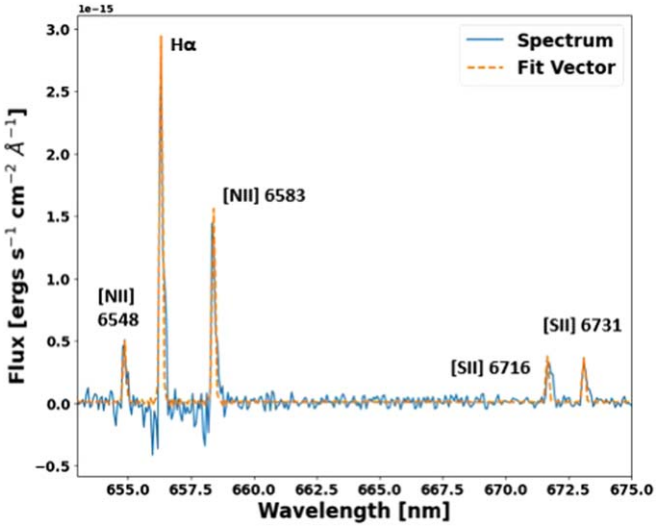

Figure 5. Example of a fitted spectrum using LUCI for a small circular region of ∼2.2 pixel radius within the filamentary nebula surrounding NGC 1275 in the central western filaments (R.A. = 3:19:49.72, decl. = +41:30:51).

function (ISF; see Martin et al. 2016) is a sinc convolved with a Gaussian resulting from the velocity dispersion along the line of sight, we used the `sincgauss` fitting model in LUCI. The results from this procedure are the amplitude, velocity, and broadening of the five emission lines present in the spectrum [S II] λ6716, [S II] λ6731, [N II] λ6584, Hα (6563 Å), and [N II] λ6548, where we separated the fitting procedure by first considering the S/N of the Hα and [N II] emission lines to obtain their respective parameters. Then, we specifically considered the [S II] emission lines to derive their own parameters, which will be detailed in Section 2.7.

Finally, to account for the location of Earth on its orbit at the time of observations, a correction is applied to the velocity map. This correction is determined with the `heliocentric_correction` function of the LUCI package, and gives a velocity correction of $-27.5\,\mathrm{km\,s^{-1}}$.

Through this analysis, we adopted a redshift of $z = 0.017284$ for NGC 1275, which LUCI uses during the fitting procedure so that all calculations are done in the rest frame of the object to determine the velocity, velocity dispersion, and flux parameters of the emission lines properly. An example of a fitted spectrum using LUCI is displayed in Figure 5. The resulting Hα flux, velocity, and velocity dispersion maps are shown in Figure 6.

Finally, through these steps, we explored the fitting of averaged spectra over the bins produced by the WVT procedure to understand better the complex nature of the ionized gas in these filaments and determine their most prominent features as if no binning was applied.

2.6. Multiple Emission Components

Due to the high spectral resolution of our observations, we have to take into account the possibility of resolving multiple velocity components that a single bin can potentially contain due to the potential overlapping of filaments (see Appendix C). Indeed, since the 3D structure of the filaments is currently unknown, it is impossible to decipher the possible overlap of several filaments.

For the sake of clarity in our resulting maps, we decided to mask the main sources of multiple emission components. First, the HV system, associated with a forefront galaxy, has a velocity of $\sim$8200 km s^{-1}. It can thus be identified through its

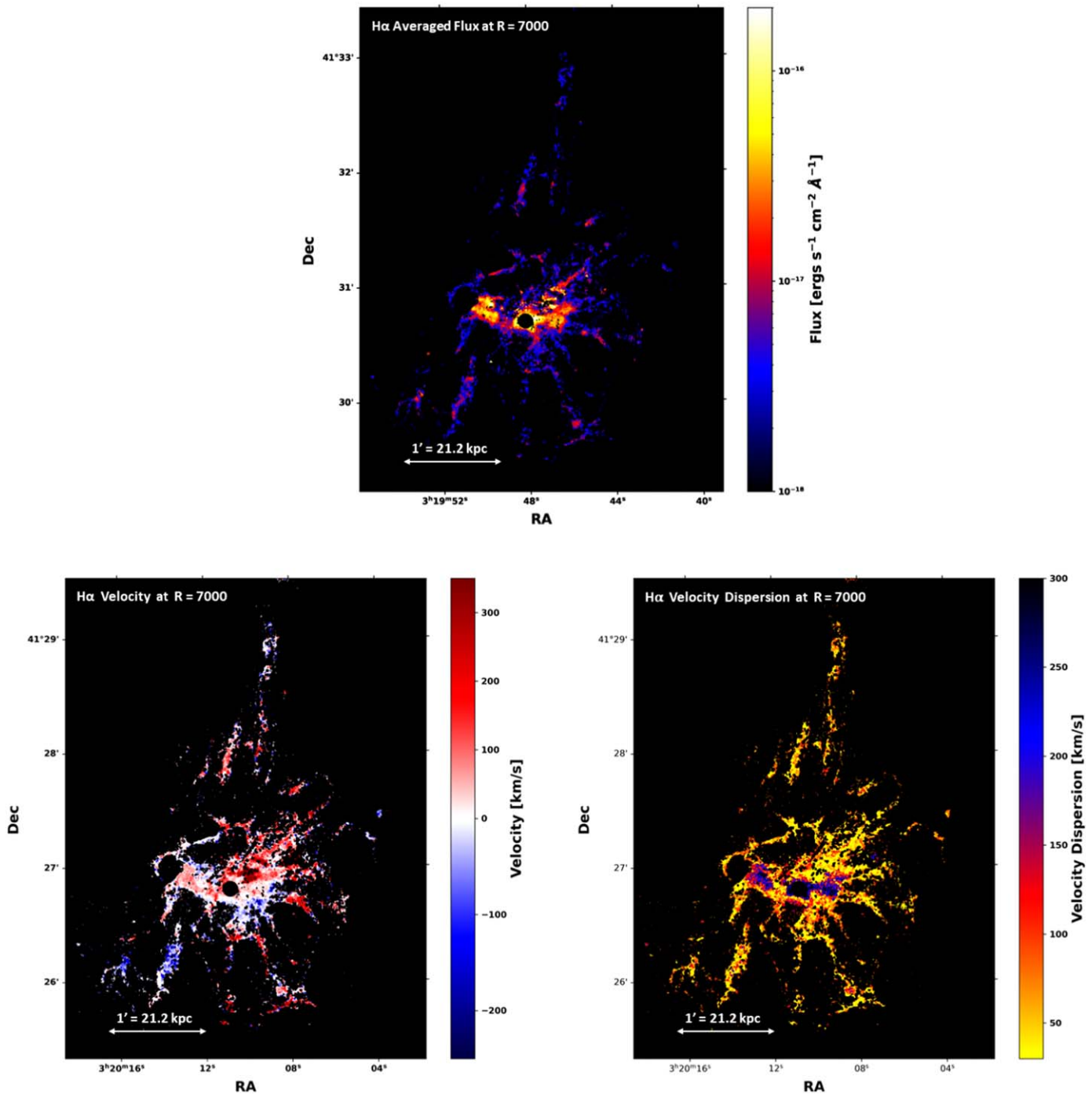

Figure 6. Top: Hα average flux map of the filaments in NGC 1275. Bottom right: Hα velocity dispersion map of the filaments in NGC 1275. Bottom left: Hα velocity dispersion map of the filaments in NGC 1275.

systemic velocity and ignored during the fitting procedure by only considering the emission lines associated with the filamentary nebula.

Moreover, broad, multiple-component emission lines from the AGN are coupled with the filament emission in the central $\sim$2.6 kpc; thus, the resulting fits produced by `LUCI` are poor when considering these specific regions. An example of a spectrum extracted from the central region close to the AGN is displayed in Figure 7.

The large broadening of the AGN's emission overlapping with the filaments' narrow emission impedes `LUCI` from properly fitting the central regions of the filamentary nebula. Indeed, the fitting algorithm proves to be limited by the presence of largely broadened and blended emission lines for which the machine-learning algorithm has not been trained on, therefore preventing it from performing accurate fitting. Therefore, to facilitate the analysis, we decided to mask the central region of emission coming from the AGN displaying broad emission lines. To do so, we studied the emission line profiles with `LUCI` and determined that the AGN spectral presence is confined within a radius of $\sim$2.6 kpc from the center of the galaxy. There was also evidence of a small

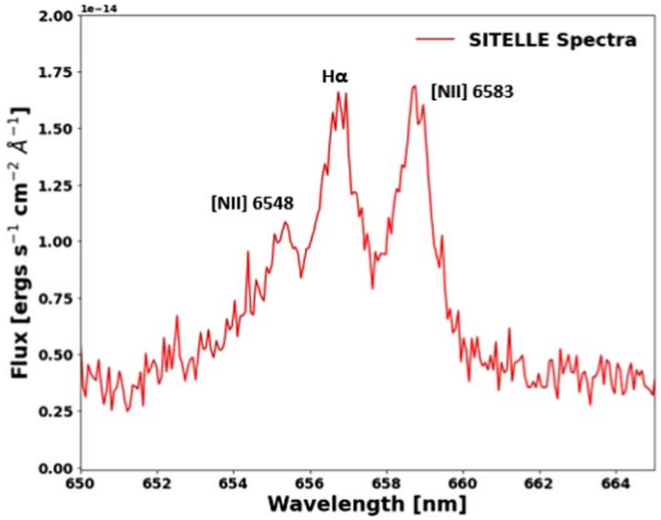

Figure 7. Example spectrum extracted from the central region of the filamentary nebula surrounding NGC 1275, centered on the AGN. Narrow emission lines overlaid on a broad component are clearly seen. This region has a radius of ∼5 pixels.

number (∼10) of localized clumps detected over 1 to 5 pixels within the central region ($r < 10$ kpc) that showed evidence of multiple components in their emission lines. Similar clumps had already been detected in a previous study by Hatch et al. (2006), where the authors mentioned the presence of several regions displaying double-peaked emission lines.

Some of these regions appear as small knots or plumes displaying an extremely low separation in velocity components, leading to slightly double-peaked emission lines. However, we can also detect slightly larger regions displaying several components in velocity and located near the eastern part of the filamentary nebula below the HV system. It is not yet clear if these regions with multiple velocity components are due to the superposition of filaments with Doppler-shifted velocities along the line of sight. Spectra of specific regions displaying several emission lines components are presented in Appendix C.

Here we focus only on the results from the fitting of a single component to all bins. A dedicated multiple-component analysis of the few localized regions with overlapping filaments, as well as of the core, will be performed in the future.

2.7. [S II] Emission Line Fitting

Regarding the detection and fitting of the [S II] λ6716 and [S II] λ6731 emission lines, one of the main difficulties in their analysis resides in the presence of strong sky lines at the same wavelengths (see Appendix A). However, after applying our methodology to tackle the background variability, we were able to detect these emission lines. To help the fitting procedure, we made new WVT bins based on S/N of the [S II] λ6716 and [S II] λ6731 doublet, which are fainter than the [N II] λ6583, Hα (6563 Å), and [N II] λ6548 lines.

The new larger bins thus created improved the detection of these fainter emission lines. The resulting [S II] λ6716 and [S II] λ6731 flux maps, velocity maps, and velocity dispersion maps are shown in Figure 8. The bottom-left and right plots clearly show similar velocity and velocity dispersion maps as the Hα seen in Figure 6. A deeper analysis of the [S II] emission line ratios, which are often used as an estimate of the gas density compared to the density of the hot X-ray gas, will be presented in a future article (B. Vigneron et al. 2023, in preparation).

3. Results and Discussion

3.1. Comparison with Previous SITELLE Observations

Previous SITELLE $R = 1800$ observations of the filamentary nebula surrounding NGC 1275 were analyzed by Gendron-Marsolais et al. (2018), who revealed several key features of its velocity structure.

Our new high-spectral-resolution observations, however, presented new challenges during the analysis step. Indeed, the spectra produced by SITELLE uses a Fourier transformation based on a sinc function, which shows specific lobes around the central peak. Since the SITELLE ISF is a sinc function convoluted with a Gaussian resulting from the velocity dispersion along the line of sight, the `sincgauss` model was specifically chosen during the spectral fitting procedure with `LUCI` to take into account the spectral information contained within the lobes properly.

Moreover, the spectral resolution associated with the SITELLE observations induces a minimum value of velocity dispersion that can be resolved clearly (see Figure 3 in Rousseau-Nepton et al. 2019). Thus, when considering a small spectral resolution of $R = 1800$ with the SITELLE instrument, as was the case for the observations studied in Gendron-Marsolais et al. (2018), the lower velocity dispersion bound that could be obtained was ∼80 km s^{-1}. However, with a high spectral resolution of $R = 7000$, the lower velocity dispersion value that can be determined is ∼15 km s^{-1}, allowing us to resolve the emission lines properly (see Figure 3 of Rousseau-Nepton et al. 2019). This result is visible in Figure 9 when comparing the spectra of the same region at both low and high spectral resolution. We can indeed observe that the width of the emission lines is smaller than what was previously found by Gendron-Marsolais et al. (2018) in regions A, B, and D. Region C is contained within the central region and given its intrinsic large velocity dispersion, the low-spectral-resolution observations of SITELLE were capable of resolving this structure.

For illustrative purposes, we also overplotted the contours of the HV system on the left-hand map of Figure 9. These contours were created by forcing `LUCI` to fit the emission line from the HV system specifically, thus allowing us to isolate it on a dedicated small region of the SITELLE data.

3.2. Emission Line Intensity Ratios and Flux Maps

First, the Hα average flux map visible in the upper plot of Figure 6 shows a disk-shaped structure in the central region with a size of ∼22 kpc by 5 kpc, displaying a flux an order of magnitude higher than the rest of the filaments. The flux map from Gendron-Marsolais et al. (2018) hinted to this structure, but the new data reveal it in much greater detail. The high average flux of this disk-shaped structure is also associated with a large velocity dispersion, which will be discussed in Section 3.4. Beyond the disk-shaped structure, localized parts of specific filaments display slightly higher Hα fluxes, but most of them have a homogeneous lower flux.

Emission line ratios can be of great interest when studying the ionization properties of an emitting gas (see Kewley et al. 2019). In this regard, the [N II] λ6583/Hα ratio is of importance since it informs us of the relative implication of soft versus hard sources

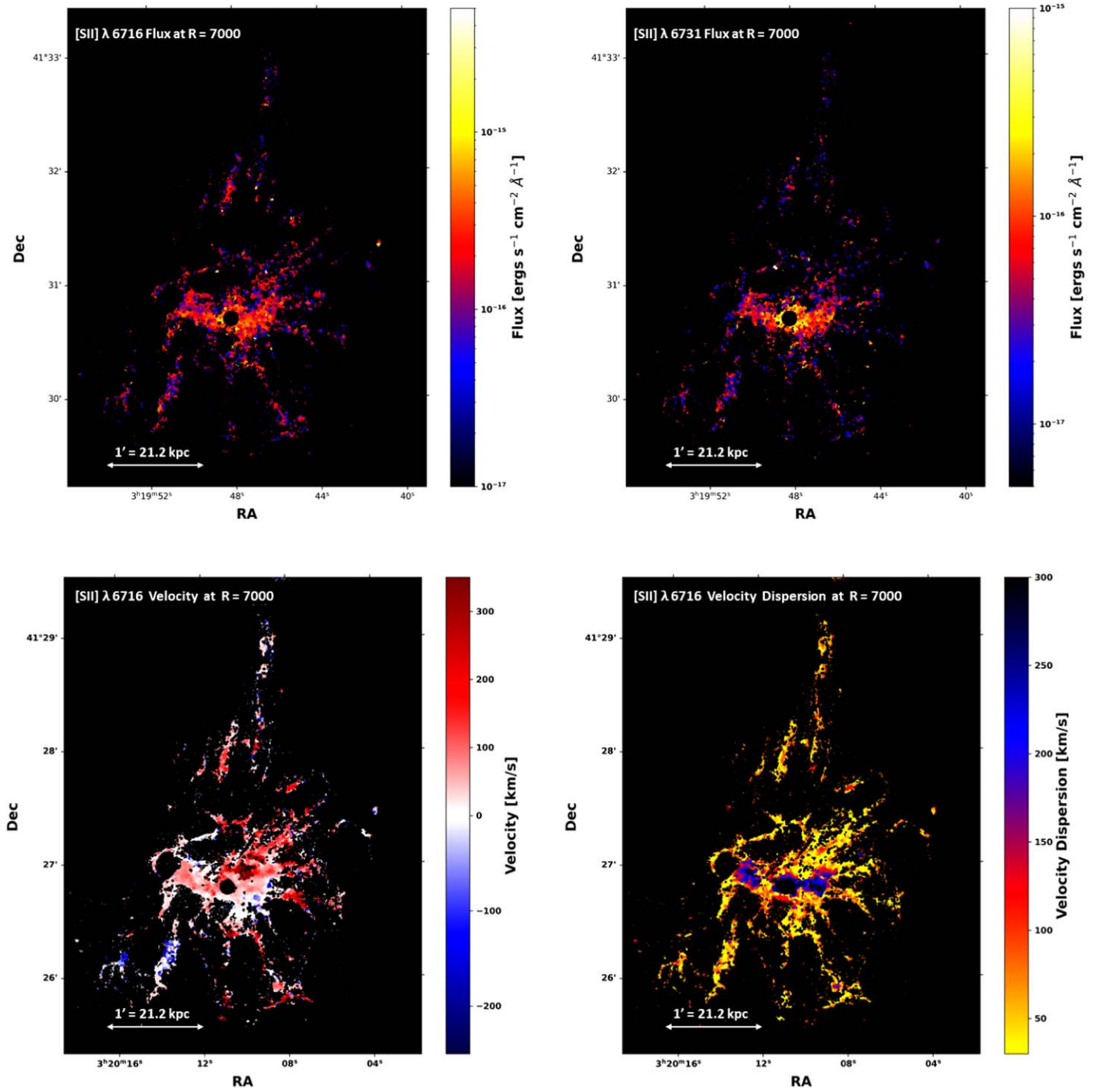

Figure 8. Upper left: [S II] λ6716 flux map of the filaments in NGC 1275. Upper right: [S II] λ6731 flux map. Bottom left: [S II] λ6716 velocity map. Bottom right: [S II] λ6716 velocity dispersion map. The velocity and velocity dispersion of [S II] λ6731 are the same as the ones for the [S II]λ6716 line since these parameters were tied when fitting the doublet.

of ionization. In the case of a low ratio (meaning Hα flux $\gg$ [N II] λ6583 flux), photons from young stars can be the ionizing source, while for a higher ratio (meaning Hα flux $\leqslant$ [N II] λ6583 flux), a harder ionizing spectrum (from an AGN, for example) or energetic ICM particles are needed to provide additional heat (see Sanchez Almeida et al. 2012). Similarly, the ratio of [S II] λ6716 to Hα (6563 Å) can be used as a confirmation value for various ionization mechanisms. Here, to produce a map of [S II] λ6716/Hα (6563 Å), we specifically applied the fitting procedure for the Hα emission line by considering the bins obtained through the WVT algorithm which uses an S/N of 35 for the [S II] doublet (between wavelengths of 6711–6757 Å), thus creating bins of the exact same size and position as the [S II] doublet flux maps but fitting the Hα emission line at $\lambda = 656$ nm. Afterwards, we can obtain the ratio map by dividing both these flux maps, therefore producing a flux

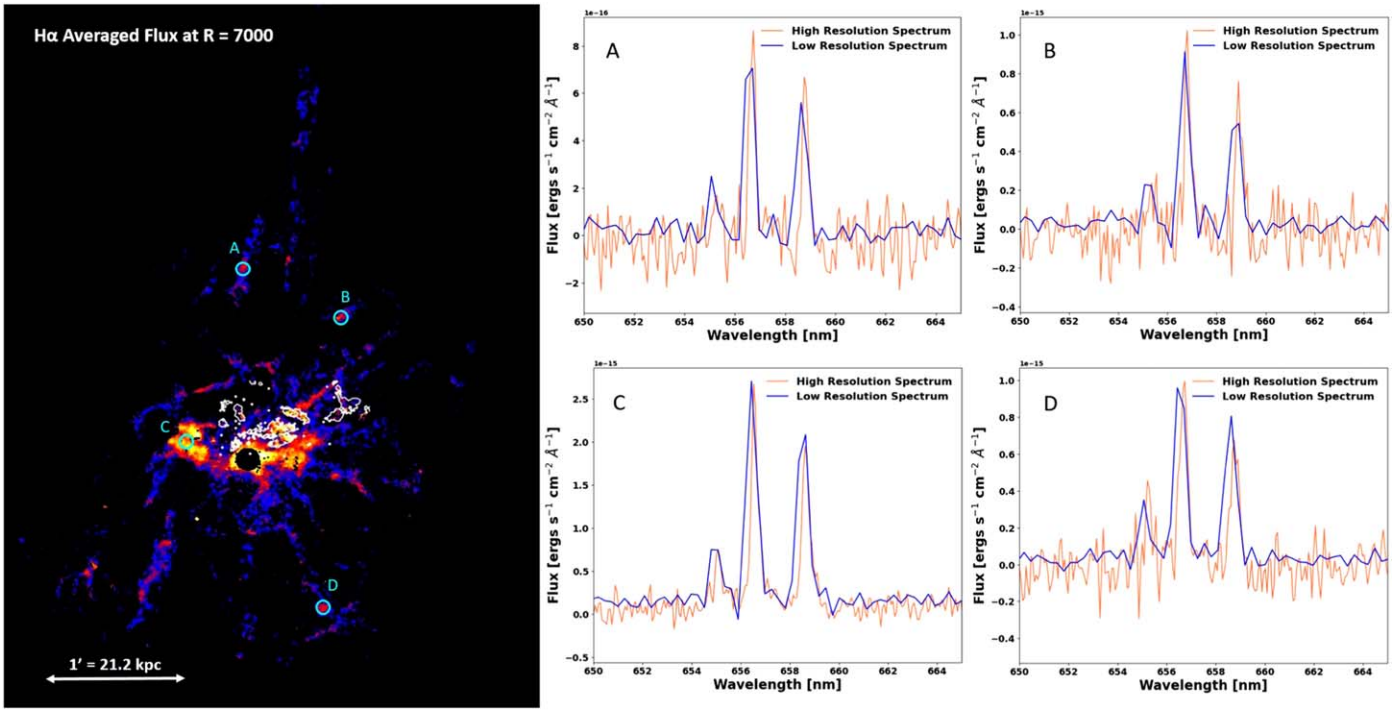

Figure 9. Comparison of the spectra extracted from four regions denoted by the letters A, B, C, and D for both low and high spectral resolution. On the left side, the high-spectral-resolution Hα average flux map is used to display the region of emission while the right side showcases the differences between the low- and high-resolution spectra. The white contours overlaid on the left-hand flux map display the HV structure situated in the forefront of the filamentary nebula of NGC 1275.

ratio map for both the emission lines with the exact same number of bins (see the bottom-left plot of Figure 10).

Figure 10 (upper-left map) shows that the central region of the structure displays a ratio of [N II] λ6583/Hα close to or slightly greater than 1.0, while the extended filaments show a variety of smaller ratio values between 0.5 and 1.0. This trend between central and extended filaments can also be seen in the upper-right plot of Figure 10, where we produced the mean (i.e., taking the mean of the ratio values across the annuli) and ensemble fit results (i.e., extracting one combined spectrum for all pixels inside the annulus and fitting it to obtain an ensemble ratio value) for the [N II] λ6583/Hα ratio across annuli containing 1500 pixels each, reproducing the work of Gendron-Marsolais et al. (2018). However, when emulating this methodology for high-spectral-resolution SITELLE data, we noticed that ensemble spectra at high spectral resolution are severely affected by the spatial distance between annuli pixels, leading to blended emission lines and to large offsets between the mean and ensemble fits. We have decided to omit those results, meaning we are analyzing only the mean fit results.

The center of each annulus is determined based on the WCS coordinates of the central galaxy NGC 1275, given as R.A. = 03:19:48.16 and decl. = +41:30:42.1 in the literature (see Gaia Collaboration 2020) and observed in our SITELLE data. The width of each annulus is determined according to the fixed number of 1500 detected pixels it contains. Therefore, the resulting annuli vary between widths of 7–10 pixels and up to 57 pixels for the outer filaments. Error bars are also plotted for both methods and obtained through statistical calculations for the mean, or through `LUCI`'s fitting procedure for the ensemble fit. The error bars for the ensemble fit have also been plotted but are too small to see compared to the data scale. This profile shows a decrease in the mean values from the center (0–10 kpc) to the outer filaments (10–30 kpc) from 1.0 ± 0.5 to 0.6 ± 0.5, respectively, thus suggesting a gradual change or variation of the ionization mechanism. However, the ratio values appear more chaotic than structured in the extended filaments, which is reflected by a fairly large standard deviation in the error bars of the mean profile (see the upper-right plot of Figure 10).

Such a radial trend is similar to what was previously found by Gendron-Marsolais et al. (2018) with low-spectral-resolution SITELLE data ($R = 1800$), and also through slit spectroscopy (Hatch et al. 2006). The presence of star formation has already been detected for specific southern and northwestern regions of the filamentary nebula (see Canning et al. 2010, 2014). However, photoionization models predict a ratio that is highly dependent on metallicity, with an upper limit of around 0.5 (Kewley et al. 2006); thus, such a process could not explain the higher ratios found throughout the southern filaments. In addition, we can also conclude that the central region, near the AGN, is more likely to be ionized by AGN activity as well as energetic particles since it displays higher ratios, while the outer filaments could predominantly be ionized by energetic particles thus showing intermediate [N II] λ6548/Hα emission line ratios.

Another possibility that is often presented as a mechanism to explain the energetics and ionization of the filaments is through collisional excitation by energetic particles coming from the hot ICM (see Ferland et al. 2009). In such circumstances, the [N II] λ6548/Hα emission line ratio would be close to $\sim$0.3. However, if we consider the ratio of [S II]/Hα, displayed in the bottom-left plot of Figure 10, we can see that the outer filaments show higher ratios above $\sim$1; nevertheless, various behavior is observed for different filaments. In the case of ionization by cosmic rays, the ratio of [S II]/Hα is predicted to

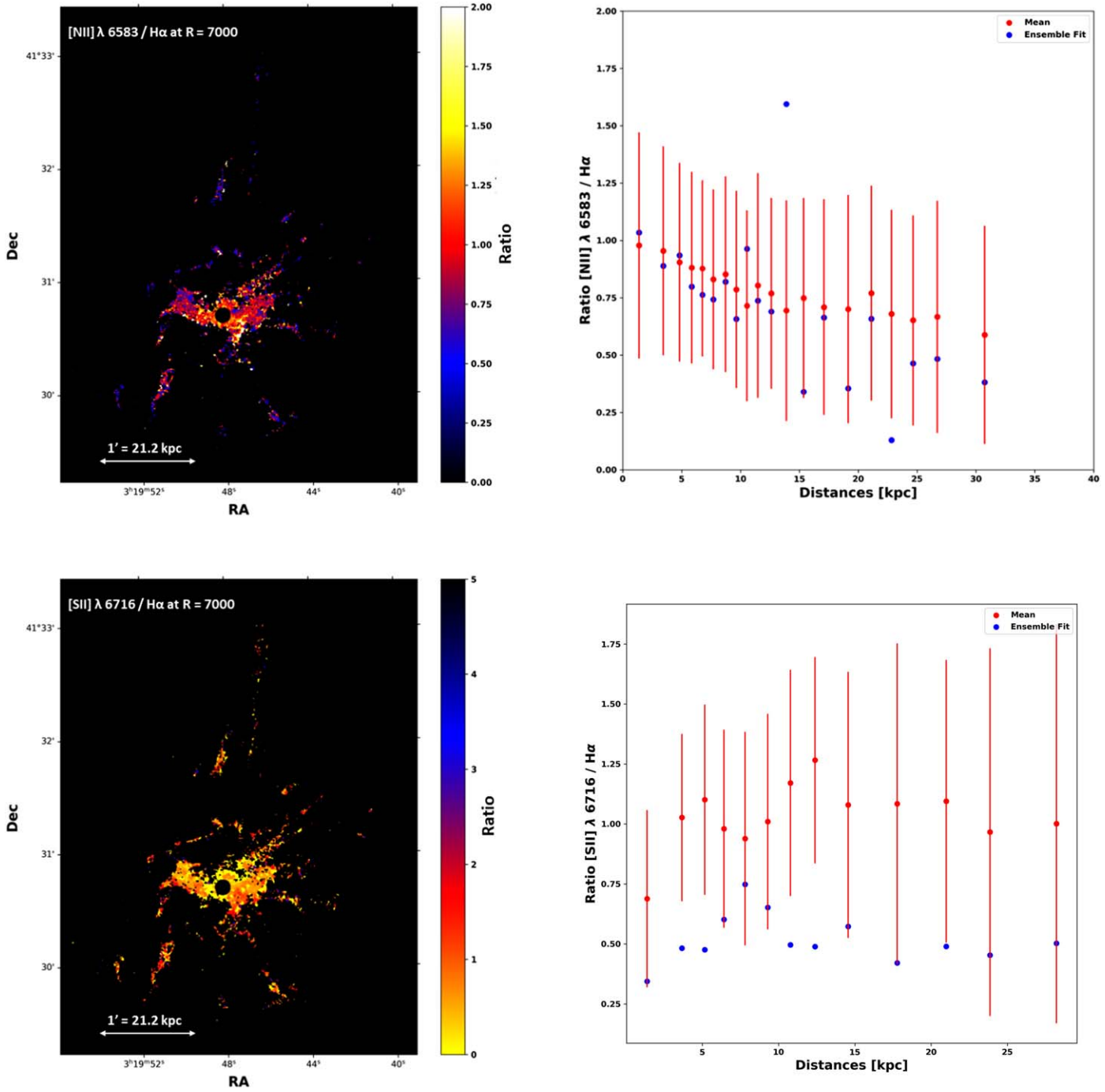

Figure 10. Upper left: [N II] λ6583/Hα ratio map. Upper right: mean (in red) and ensemble fits (in blue) across annuli containing 1500 pixels for the [N II] λ6583/Hα ratio. The error bars for the ensemble fit have been plotted but are too small to see compared to the data scale. Bottom left: [S II] λ6716/Hα ratio map. Bottom right: mean (in red) and ensemble fits (in blue) across annuli containing 1500 pixels for the [S II] λ6716/Hα ratio. The error bars for the ensemble fit have been plotted but are too small to see compared to the data scale.

be 1.4 according to the cosmic-ray heating model (see Table 5 of Ferland et al. 2009), which could be an argument in favor of the collisional ionization model for the outer filaments. However, the northern filaments as well as parts of some other filaments show even higher [S II]/Hα ratio values above $\sim$2.0. Nevertheless, in the bottom-right plot of Figure 10, we produced the mean and ensemble fit results of the [S II] λ6716/Hα ratio across annuli containing 1500 pixels each. We can see that most mean values are constrained between $\sim$0.5 and 1.5, which could argue in favor of an ionization mechanism through cosmic rays, though it is not possible to offer conclusive results with the emission lines at hand.

Using subsequent SITELLE observations with the SN1 (365–385 nm) and SN2 (480–520 nm) filters of NGC 1275 (PI: G. Marsolais), that provide other emission lines, we are currently pursuing a deeper analysis of the ionization mechanisms at play in the filamentary nebula (C. L. Rhea et al. 2023, in preparation). Similarly, the analysis of [S II] emission lines and their ratios will be explored in a future article (B. Vigneron et al. 2023, in preparation).

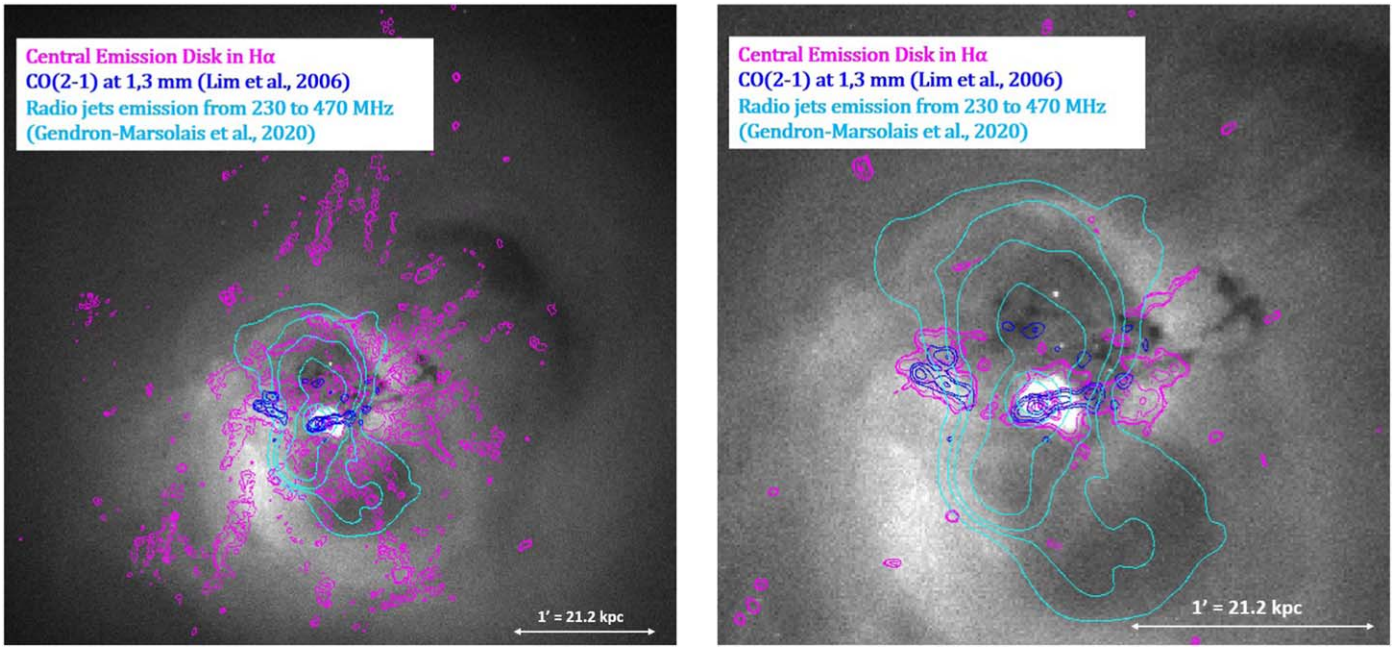

Figure 11. Left: Chandra 0.5–2.0 keV observations of NGC 1275. The magenta contours show the Hα filaments as observed with SITELLE at high spectral resolution at a flux level starting at 1×10^{-18} erg s^{-1} cm^{-2} Å^{-1}. The cyan contours display the radio emission from 0.23 to 0.470 GHz as observed with the Very Large Array (Gendron-Marsolais et al. 2020), tracing the radio jets. The blue contours represent the CO(2−1) central emission disk-shaped structure as observed with the SMA (Lim et al. 2008). Right: zoomed-in image of the left-side figure with an Hα flux cutoff of 1×10^{-17} erg s^{-1} cm^{-2} Å^{-1}.

3.3. Central Disk-shaped Structure

As we mentioned, the filamentary nebula seen in the optical is part of a larger multiphase structure that correlates spatially with filament-like structures seen in X-rays (Fabian et al. 2003, Walker et al. 2015) and molecular gas structures (Salomé et al. 2008, Ho et al. 2009) Such multiphase filaments are at the heart of many models explaining the formation of such structures. Indeed, it is argued that the jets of the central SMBH create expanding bubbles, rising through and carving the ICM, while inducing turbulence, sound waves, and shocks (e.g., Dhawan et al. 1998; Falceta-Gonçalves et al. 2010). This effect can be seen through the deformation of optical filaments taking the shape of convection cells and their spatial correlation with the trailing radio bubbles (Fabian et al. 2003; see also the horseshoe filament in the left plot of Figure 11).

One model argues that the depletion of metals in the galaxy and the deformed morphology of these filaments are explained by the rise of bubbles fueled by the activity of the central SMBH (e.g., McNamara & Nulsen 2007).

A second model demonstrates that the rising of radio bubbles through the ICM can trigger local thermal instabilities in the X-ray–emitting gas that would lead to local cooling flows, where the density of material increases as a consequence of cooling. Due to the intense gravitational potential of the BCG, these filaments of cooler gas fall onto the BCG, fueling the black hole activity through this feedback cycle (e.g., Voit et al. 2017; Tremblay et al. 2018). This precipitation-based model could explain the observed multiphase structure by the cooling of gas from X-ray temperatures at $\sim 4 \times 10^7$ K, down to cold molecular gas at $<10^3$ K visible in radio (McNamara et al. 2016, Dutta et al. 2022). Thus, the detection of a cold CO(2−1) molecular gas structure close to the central region of the filaments in NGC 1275, as well as similar detections of correlated cold molecular gas in the outer filaments (Salomé et al. 2011) offer a key argument regarding this formation model. The strongly emitting central structure was detected and studied by Lim et al. (2008) and is divided into three main filaments and smaller clumps, all located near the central plane of the galaxy. They also showed that this central disk spatially correlates with the optical filaments seen in Hα, as well as the X-ray emission between 0.5 and 2.0 keV. The X-ray image shown in Figure 11 was obtained by combining several Chandra observations between 0.5 and 2.0 keV and correcting the exposure of the background subtracted image. The exposure time is comprised between 800 ks and 1 Ms. Our new observations with SITELLE as seen in Figure 11 also show that the Hα flux contours spatially correlate with the CO(2−1) molecular gas as seen by Lim et al. (2008), especially in the case of the left-side filaments of the central disk-shaped structure (see the right panel of Figure 11), while also located along the lower borders of an expanding radio-filled bubble as observed by Gendron-Marsolais et al. (2020). This region seems to be directly linked with the central disk that has a higher average flux and velocity dispersion as seen with the Hα flux map shown in Figure 6.

Such contrast between the central and extended flux is similar to what was previously obtained by Salomé et al. (2011), where the detection of CO across the filaments demonstrated that the central region has a flux around 10 times higher than the emission found in the filaments. However, Lim et al. (2008) clearly showed that this higher central flux emission is not only linked to the AGN, but also to this bright and uniform disk-shaped feature. This result proves insightful when considering the observations of BCGs by the Atacama Large Millimeter/submillimeter Array (ALMA; Russell et al. 2019) revealing mostly filamentary and disk-shaped structures around these galaxies. Some of these features

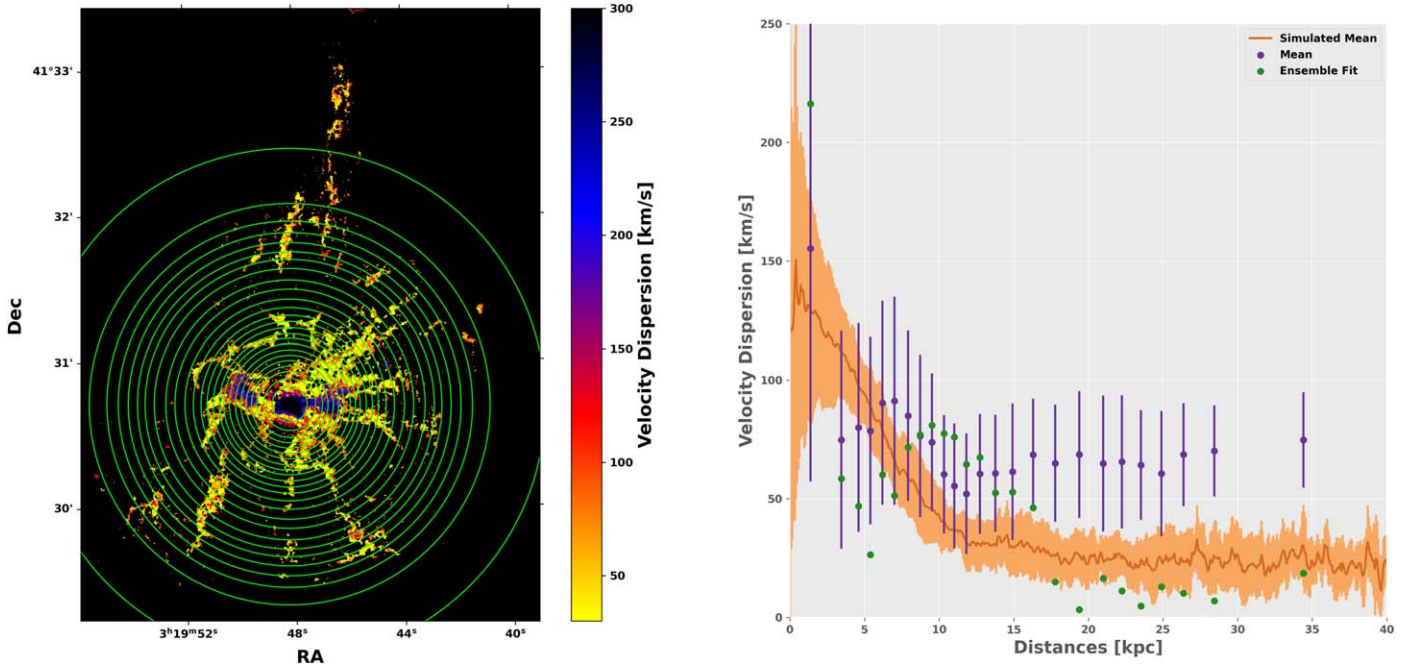

Figure 12. Left: Hα velocity dispersion map. Right: mean (in purple) and ensemble fits (in green) across annuli containing 1500 pixels for the Hα velocity dispersion. The error bars for the ensemble fit have been plotted but are too small to see compared to the data scale. Simulation results of the velocity dispersion in the optical filaments of the Perseus Cluster. The brown line shows the average line-of-sight velocity dispersion as a function of radius in the simulated Perseus cluster from Li et al. (2015), while the 1σ scatter is shown though the orange shaded area.

display rotation (e.g., Hamer et al. 2014), however, this does not appear to be the case for the central disk-shaped structure of NGC 1275 (see Lim et al. 2008), even though closer observations of the inner regions close to the central galaxy indicate rotational motion of the gas (see Nagai et al. 2019; Riffel et al. 2020).

Decades of optical observations have revealed that NGC 1275 is surrounded by an extended array of filaments spreading throughout the inner 100 kpc and are the largest seen in any cluster (e.g., Conselice et al. 2001). However, we also know that the Perseus cluster is one of the closest to us; therefore, in more distant clusters, only the brightest filaments could potentially be seen. Indeed, when considering our renewed observations of NGC 1275 with SITELLE, we can observe a significantly brighter central disk-shaped structure ($\sim 1 \times 10^{-17}$ erg s^{-1} cm^{-2} Å^{-1} flux) as opposed to the outer filaments ($\sim 1 \times 10^{-18}$ erg s^{-1} cm^{-2} Å^{-1} flux). Thus, more distant clusters could also harbor extended arrays of filaments that our current generation of telescopes are not able to detect. Simulations exploring this idea have been developed for NGC 1275 by McDonald et al. (2010) and revealed that by a redshift of $z \sim 0.06$, most of the filaments would be undetectable, leaving only the central bright region surrounded by unresolved features (see Figure 16 of McDonald et al. 2010). Similarly, recent observations of the BCG of the Centaurus cluster by Fabian et al. (2016b) revealed a faint and diffuse Hα nebula surrounding it.

Recent ALMA observations of NGC 1275 obtained by Nagai et al. (2019) provided a detection of a smaller portion of the central disk in CO(2−1) close to the AGN, as well as HCN (3−2) and HCO$^+$(3−2) emission within a radius of 1.″8 (0.658 kpc) around the AGN, revealing rotating motion of the emitting gas at this scale. This detection is within the central region that we have masked in our SITELLE fits due to the broad component being present, as mentioned in Section 2.6.

3.4. Velocity Dispersion Structure

Previous observations of the filamentary nebula surrounding NGC 1275 with slit spectroscopy or IFU instruments demonstrated that the velocity dispersion of the ionized optical gas is higher in the central region near the AGN ($\sim$150 km s^{-1}) while diminishing gradually to lower values ($\sim$50 km s^{-1}) in the outer filaments (Hatch et al. 2006, Gendron-Marsolais et al. 2018). These observations support the idea that the AGN activity is the source of a higher level of agitation in the central region while other mechanisms such as the turbulence and shocks induced by the trailing of ascending radio-filled bubbles induce a lower but nonnegligible velocity dispersion in the outskirts of the structure (Falceta-Gonçalves et al. 2010).

The new SITELLE observations at high spectral resolution confirm that the central disk-shaped structure with higher velocity dispersion is not due to multiple velocity components based on visual inspection of the spectra. Indeed, the regions displaying multiple velocity components are extremely localized compared to the extended disk-shaped central structure visible in Figure 6. Beyond this disk-shaped structure, the velocity dispersion decreases sharply and remains uniformly low throughout the rest of the filaments, out to $r \sim 50$ kpc. The central velocity dispersion is almost two times higher in the central disk-shaped structure than what previous low-spectral-resolution observations showed (Gendron-Marsolais et al. 2018, see left plot of Figure 12). When considering only the central bright region by applying a more stringent flux cutoff of 1×10^{-17} erg s^{-1} cm^{-2} Å^{-1}, the mean velocity dispersion of the central disk-shaped structure is $\sim$134 km s^{-1}. The disk-shaped structure seems specifically located at the position of

the central CO(2−1) disk of molecular gas and at the border of the inflating radio bubble (see the right side of Figure 11).

The most striking feature displayed in Figure 12 is the lack of a smooth gradient between the high dispersion of the central region ($\sim$134 km s^{-1}) and the lower dispersion of the outer filaments ($\sim$44 km s^{-1}; see also the right plot of Figure 12). For the gas in the central region, we could expect to see a higher velocity dispersion since more gas is likely found near the central regions, whereas for the outer filaments, we are viewing individual filaments and therefore, we are probing more of a pencil beam view of the kinematics in the outer filaments. However, the sharp contrast in velocity dispersion from the central disk-shaped structure to the filaments beyond this structure is puzzling. We also note that despite this expected overlap of gas in the central region, few highly separated velocity component emission lines are found in this region, which will be discussed in Section 3.6.

If we consider the entire system of low dispersion filaments, it has a global velocity dispersion much greater than $\sim$44 km s^{-1}, as indicated by the Hα velocity dispersion map, even if the central region displaying higher values is excluded. The uniformity in the (pencil beam) velocity dispersion of the outer filaments might therefore be reflecting a different physical process from the one responsible for the global velocity dispersion of the filament system.

The global velocity dispersion is likely to be connected to motions of the hot medium, while the pencil beam velocity dispersion of the ionized gas is more likely to be connected to shearing motions at the interfaces between the filaments and the hot medium, which we will investigate in Section 3.5.

Thus, this result could also imply that two completely different mechanisms might be at play to introduce such a clear differentiation in velocity dispersion.

We also compare our result with simulations from Li et al. (2015; see Figure 12). The brown line shows the average line-of-sight velocity dispersion as a function of radius in simulated filaments from Li et al. (2015) that reproduce the ones seen in NGC 1275. We first take the simulation outputs generated every 10 Myr over a 300 Myr period when the simulated cluster most resembles Perseus in the morphology and spatial distribution of the Hα filaments. For each output, we make a line-of-sight velocity dispersion map of the Hα gas (with temperatures of $\sim 10^4$ K) weighted by emissivity. Then, the data are split into radial distance bins and averaged for each bin. We then compute the time-averaged velocity dispersion profile and its 1σ scatter (orange shaded area). We can thus see that the simulation shows lower values of velocity dispersion further away from the central region, which is in accordance with our observational results. Overplotted in purple and green are, respectively, the mean and ensemble fits extracted from the annuli seen in the left side of Figure 12. These data points clearly show a drop in velocity dispersion at a short radial distance away from the central region and matching the simulated data. The outer filaments display stable low velocity dispersion in agreement with the simulated data.

An interesting similarity to our results can be observed in the study of A2597 by Tremblay et al. (2018), as observed with MUSE and ALMA. This study also demonstrated the presence of a spatial correlation between a central v-shaped molecular gas structure and its optical emission counterpart in Hα. Both of these structures were also found to be comoving and closely tracing the wake of the X-ray cavities formed by the activity of the BCG's AGN. Moreover, when considering the velocity dispersion of the optical gas in A2597 (see Figure 13 of Tremblay et al. 2018), a similar result can be observed where the correlated emission region displays an extremely high velocity dispersion (up to $\sim$350 km s^{-1}), which quickly falls to lower values for the outer filaments ($\sim$50 km s^{-1}), can be seen.

Regarding the filament formation models that have been developed and detailed previously, Tremblay et al. (2018) explore a unified model involving chaotic cold accretion, precipitation, and stimulated feedback through the description of a galaxy-scaled "fountain." In this model, the central cold molecular gas and optically emitting filaments supply an accretion reservoir to the AGN, thus fueling its activity. The jets it produces then inflate radio bubbles, buoyantly rising and carving the surrounding ICM, therefore creating turbulence and thermal instabilities as well as uplifting ionized gas in their trail (e.g., Li & Bryan 2014a; McNamara et al. 2016). The raised material then precipitates back to the central potential well thus sustaining the "fountain." Moreover, further thermal instabilities generated by turbulent AGN feedback reinforce the precipitation of colder gas in slightly denser parts of the ICM, thus facilitating the formation of extended filamentary nebulae (e.g., Voit 2018; see also McNamara et al. 2014; Russell et al. 2019).

3.5. Extended Filaments and Turbulent Radiative Mixing Layers

We now investigate a possible formation scenario for the extended filaments displaying lower velocity dispersion through turbulent radiative mixing layers. This scenario involves the formation of filaments in situ instead of being dragged out by the adiabatic rise of the radio bubbles carved by the SMBH jets.

Turbulent mixing layers are frontier layers between gaseous material at different temperatures. Due to their extreme difference in internal energy, the materials will interact and produce a layer of intermediate temperature where turbulent motions are more prominent. This layer will thus produce emission lines associated with the intermediate temperature and possibly shield the inner colder layer from being completely mixed with the higher-temperature material. In the context of filaments in clusters, the hot intracluster gas at $\sim 4 \times 10^7$ K (Hitomi Collaboration et al. 2016) acts as a warm layer while turbulent motions are thought to be due to AGN feedback processes and set a frontier layer between this medium and the colder optically emitting filaments at 10^4 K.

Previous work by Begelman & Fabian (1990) has highlighted the idea of extended turbulent mixing layers in the ICM. They discussed that filamentary structures visible in the optical could form out of the cooling flows of AGN through absorption of far-ultraviolet emission of turbulent mixing layers, which would then induce UV and optical emission via photoionization of the colder gas. However, detections of embedded cold molecular gas all throughout the filamentary nebula were made later by Salomé et al. (2006), implying that turbulent radiative mixing layers could be created at the boundaries between cold molecular gas and the surrounding hot ICM.

Indeed, the ICM of the Perseus cluster is known to have a high temperature ($\sim 4 \times 10^7$ K; see Hitomi Collaboration et al. 2016), while the cold molecular gas found all throughout the filaments has a much lower temperature ($\sim$10–10^3 K; e.g.,

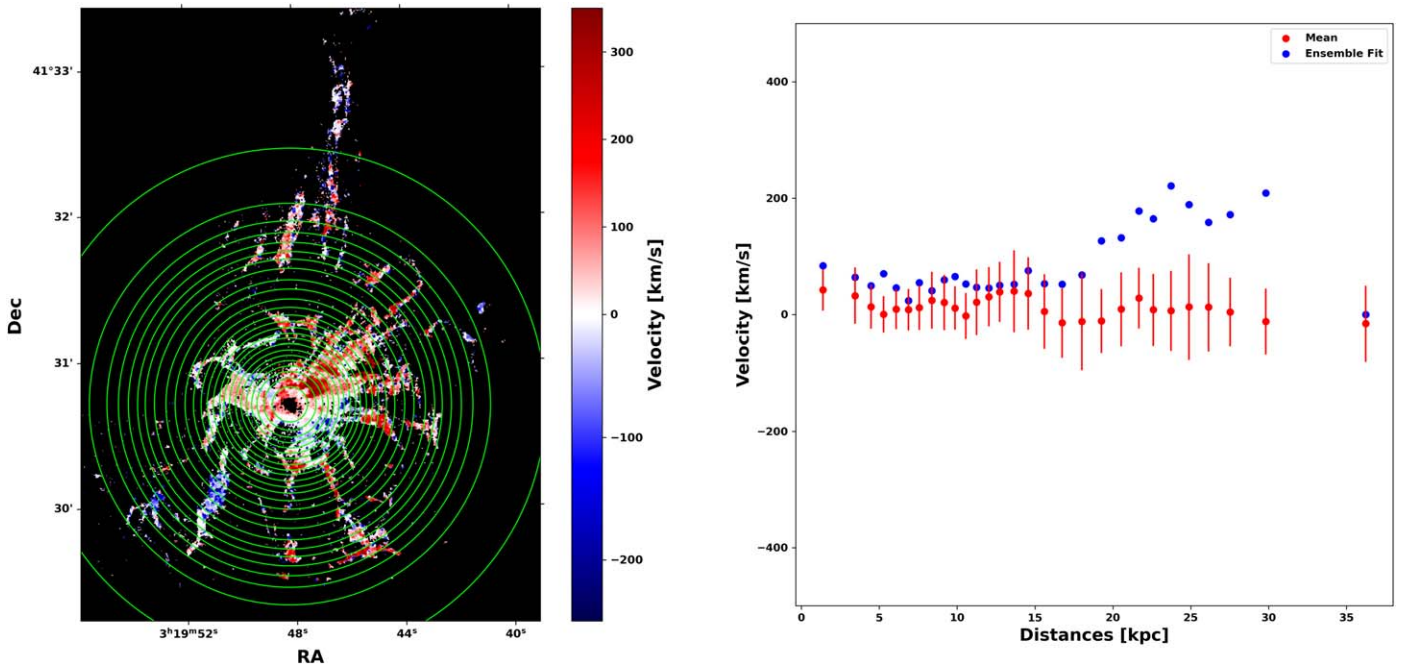

Figure 13. Left: Hα velocity map. Right: mean (in red) and ensemble fits (in blue) across annuli containing 1500 pixels for the Hα velocity. The error bars for the ensemble fit have been plotted but are too small to see compared to the data scale.

Salomé et al. 2011). Thus, we might wonder if the optical emission observed with the SITELLE data could be part of a radiative turbulent mixing layer between the two media. The presence of a turbulent mixing layer could then explain the intermediate temperature of the optical gas.

We do know that the filaments are extremely thin and display a thread-like structure (Fabian et al. 2008, 2016a), which would be reminiscent of the shape taken by turbulent mixing layers (see Abruzzo et al. 2022). With such a thin structure, physically close filaments must be connected, leading to single-component emission lines (see Hatch et al. 2006). A spectral resolution higher than $R = 7000$ would be needed to explore in detail the possible multiple components of their emission lines since none are detected within the outer filaments after spectral examination of the SITELLE data.

The velocity dispersion in mixing layers is increased by in situ turbulence caused by interactions between material at different temperatures. Recent simulations (e.g., Ji et al. 2019; Abruzzo et al. 2022; Fielding & Bryan 2022) show, however, that the turbulence of material inside the layer remains low ($\sim$30 km s^{-1}.). These simulation results could potentially prove insightful with regards to the observed mean velocity dispersion value of $\sim$44 km s^{-1}, prevalent within the extended filamentary nebula surrounding NGC 1275.

Hence, when considering the structure of a turbulent mixing layer in conjunction with our optically emitting extended filaments, it could mean that the outer layer of turbulence between the cold molecular gas and the hot ICM could be shielding the inner filaments and preventing them from having a higher velocity dispersion, leading to a clear dichotomy between the inner filaments, disturbed by the formation and growth of radio bubbles, and the outer quiescent filaments. Therefore, the velocity dispersion in the outer extended filaments could be a proxy for turbulent radiative mixing layers.

Finally, recent works reported the discovery of hidden cooling flows in a sample of nearby clusters of galaxies, including Perseus (see Fabian et al. 2022, 2023a, 2023b). Here, the authors argue that AGN feedback may not be as efficient in heating the ICM as initially thought; instead, the ICM would be allowed to cool, explaining the substantial molecular gas reservoirs found in these systems. They predict that these cooling flows are not seen at X-ray wavelengths because they are being obscured by photoelectrically absorbing cold clouds and dust (e.g., White et al. 1991; Johnstone et al. 1992; Fabian et al. 1994)—if this is the case, then the absorbed emission will reemerge in the FIR.

Indeed, extreme cooling of the gaseous material surrounding BCGs could prohibit them from being detected due to extremely low temperature and emissivity (see Fabian et al. 2023a). According to these results, cooling flows of $\sim$30–100 $M_{\odot}$ yr^{-1} could therefore be present within clusters such as the Perseus cluster of galaxies (Fabian et al. 2022). Interestingly, it is suggested that these hidden cooling flows could have internal structures resembling that of turbulent radiative mixing layers, similar to those proposed here (see Begelman & Fabian 1990; Fabian et al. 2023a). Nevertheless, future observations of the ICMs in clusters of galaxies with upcoming X-ray telescopes such as XRISM will probe a variety of transitions expected from such hidden cooling flows, providing further insight into these flows and their connection to multiphase gas in clusters.

3.6. Velocity Structure

Now focusing on the analysis of the velocity structure obtained with the new SITELLE observations, we find a very similar Hα velocity map as to what was previously obtained by Gendron-Marsolais et al. (2018) with lower-spectral-resolution observations (see Figure 5 of Gendron-Marsolais et al. 2018; the left plot of Figure 13). This result strengthens previous conclusions regarding the dynamics of the filamentary nebula.

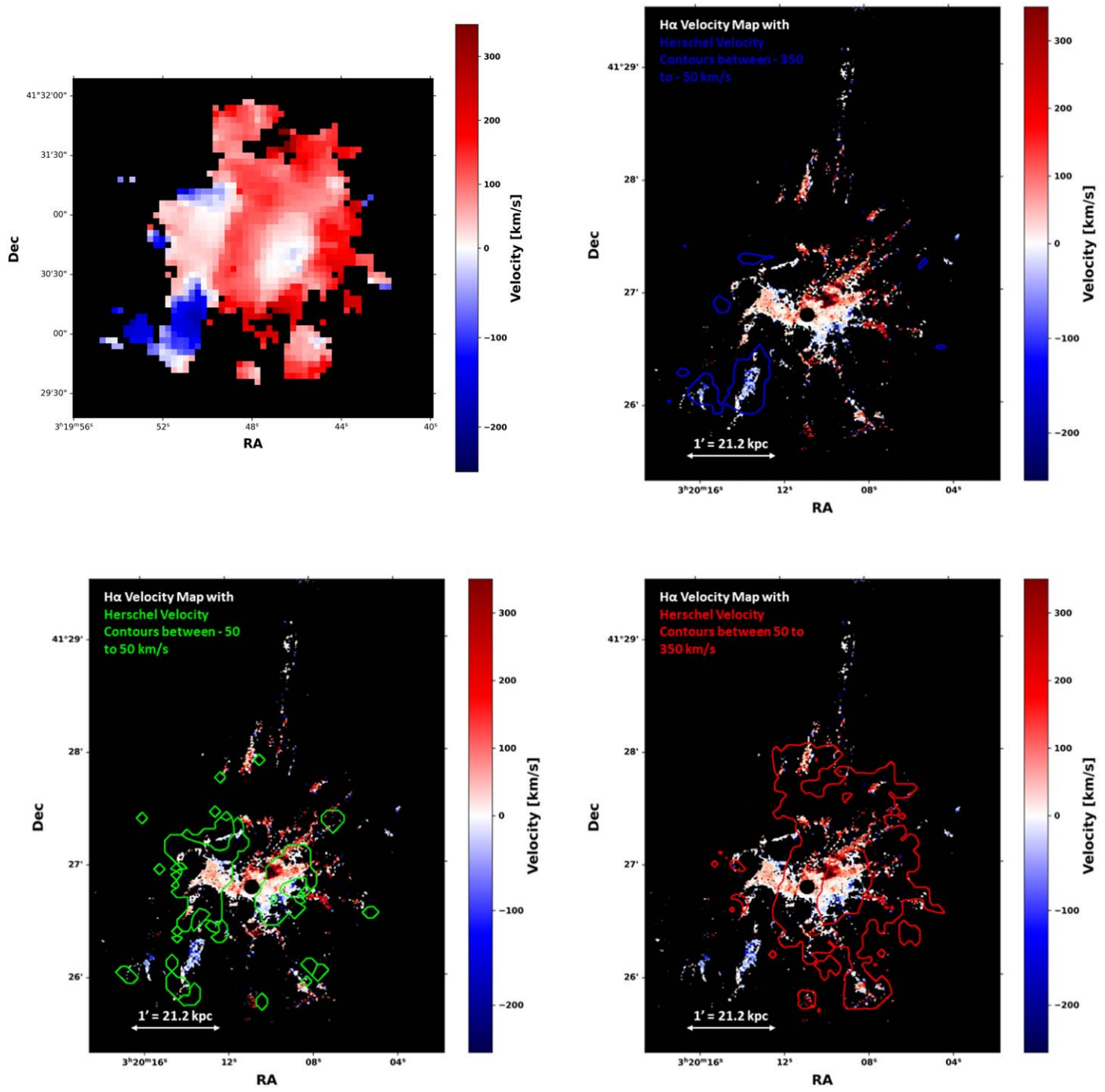

Figure 14. Upper left: Herschel Infrared Space Observatory [C II] emission line velocity map corrected for a redshift of $z = 0.017284$ (Mittal et al. 2012). Upper right: Hα velocity map as obtained with SITELLE data at high spectral resolution overplotted with contours of Herschel velocity between -350 and -50 km s^{-1}. Bottom left: Hα velocity map as obtained with SITELLE data at high spectral resolution overplotted with contours of Herschel velocity between -50 and 50 km s^{-1}. Bottom right: Hα velocity map as obtained with SITELLE data at high spectral resolution overplotted with contours of Herschel velocity between 50 and 350 km s^{-1}.

Moreover, when looking at the mean and ensemble velocity fits across annuli containing 1500 pixels (see the right plot of Figure 13), there does not appear to be a specific radial velocity trend throughout the filaments, which reinforces the idea of a chaotic velocity structure.

Considering the Herschel infrared emission kinematics studied by Mittal et al. (2012) and displayed in the upper-left panel of Figure 14, we can see that similar velocity trends could also hint at a comoving nature of the gas at various wavelengths. Indeed, when considering similar velocity intervals as shown in Figure 5 in Mittal et al. (2012), we can clearly see that the southwestern filament's kinematics (see the top-right plot of Figure 14) display a similar trend of negative velocities between -350 and -50 km s^{-1} with the spatially correlated [C II] emission line kinematics (see the top-left plot of Figure 14). This trend is also visible for both intermediate

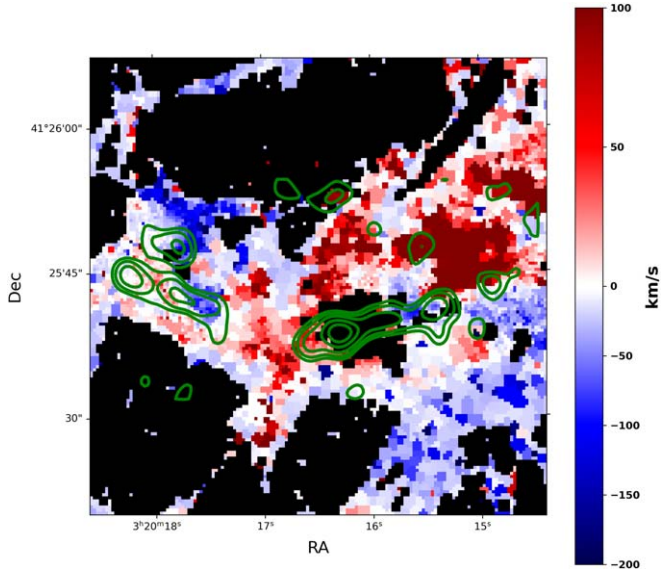

Figure 15. Velocity map in Hα and [N II] of the central region of the filamentary nebula shifted to a redshift of $z = 0.01756$ in order to match the study of Lim et al. (2008). The contours of the central disk observed in CO(2−1) with the SMA by Lim et al. (2008) are superimposed in green.

velocity values between −50 and 50 km s^{-1} as well as positive velocities between 50 and 350 km s^{-1}, although less strikingly (see the bottom plots of Figure 14).

Lim et al. (2008) also obtained a velocity map of the central molecular gas disk, which showed mostly blueshifted velocities and no sign of global rotation. To compare directly the velocity maps obtained for the optical emission to the molecular map, we shifted our map considering the redshift value of $z = 0.01756$ used by Lim et al. (2008) instead of the adopted $z = 0.017284$. After this correction, the Hα emission shows a similar velocity structure for the central disk-shaped structure (see Figures 15 and 2 of Lim et al. 2008).

The detection of similar disk-shaped structures can also be found in simulation works such as those done by Li & Bryan (2014b), where they exhibit higher levels of flux and originate from the cooling of gas onto the black hole's potential well. However, the main difference to these simulations is the fact that the central disk always displayed a rotating motion along the plane perpendicular to the jets, which is not the case for our observations where the motion seems more chaotic (see Figures 13 and 15). This difference shows that these simulations seem not to be fully capturing the physical processes at play in the formation and evolution of the filaments we are observing in NGC 1275. Moreover, the presence of radio bubbles fueled by the SMBH relativistic jets, which seem spatially linked to the presence of this disk, was not considered in previous simulations until recently (see Yang et al. 2019). However, these simulations incorporating the effect of expanding radio bubbles do not yet study their impact on the velocity dispersion and kinematics of the surrounding medium of the bubbles. This aspect of 3D hydrodynamical simulations of AGN feedback still needs to be explored to understand properly the prominent role of radio bubbles on their surrounding environment.

In that sense, the recent simulation works by Zhang et al. (2022) clearly show turbulence and eddy formation as well as the uplift of material in the wake of rising radio bubbles. Though the simulation models only involve detached bubbles approaching their terminal velocities, it is still of interest to see that material close to the central region gets lifted upward and acts as the upper layer of the deformation close to the bubble's lower boundary (see the top panels of Figure 4 in Zhang et al. 2022). Therefore, an argument could be made that the central region or disk visible in our observations, displaying a higher level of velocity dispersion as well as a clear spatial correlation to cold molecular gas, could be lifted through the detachment and adiabatic rise of the bubbles, thereafter forming future filamentary structures around NGC 1275.

Thanks to the high spatial and spectral resolution of SITELLE, we can also study the velocity profiles of targeted filaments in their entirety. To do this, we extracted velocity measurements and the mean within 10 bins over some specific filaments as in Gendron-Marsolais et al. (2018). Figure 16 shows that the velocities of the outer filaments are significantly more heterogeneous and chaotic, while the velocities of the central disk display less variations. Its velocity profile could also hint at a potential rotation pattern in the central radius of 2.5 kpc around the AGN, however, the error bars prevent us from making a clear conclusion.

The northern filament displays a velocity profile ranging from slightly positive to slightly negative values the further away from the base of the filament, which would indicate stretching. Similar results were obtained both with SITELLE (Gendron-Marsolais et al. 2018) and the Gemini Multi-Object Spectrograph (Hatch et al. 2006). The southern filament mostly shows negative velocities that slightly decrease then increasing along the filament, while the central filament seems to display an inverse trend with mostly positive velocity values. If we now bring our attention to the average velocity profile of the Horseshoe filament, we can see that both its bases (first and last data points of the lower-left panel of Figure 16) seem to display an average velocity closer to negative velocities of ∼−25 km s^{-1} while the tip of the Horseshoe (represented by the fifth and sixth data points of the lower-left panel of Figure 16) also display a drop in average velocity closer to zero velocity. On the other hand, the branches of the Horsehoe clearly display positively increasing then decreasing average velocity values (as shown in the lower-left panel of Figure 16). This average velocity profile could indicate that the branches of the Horsehoe filament might be stretching horizontally as opposed to the bases and tip, which seem to follow a trend of displacement through the traction of a radio-emitting bubble (see Hatch et al. 2006). However, the limited detection of the tip of the Horseshoe, as can be seen on the right-hand side of Figure 16, prevents us from making conclusive statements regarding these central bins of the Horseshoe average velocity profile.

4. Conclusion

We performed an analysis of new high-spectral-resolution observations with SITELLE and obtained new flux, velocity, and velocity dispersion maps of [S II] λ6716, [S II] λ6731, [N II] λ6584, Hα (6563 Å), and [N II] λ6548 emission lines of the filamentary nebula surrounding NGC 1275, the BCG of the Perseus cluster.

1. We detected a central disk-shaped structure displaying a higher average flux (∼1×10^{-17}–2×10^{-16} erg s^{-1} cm^{-2} Å^{-1}) and velocity dispersion (∼134 km s^{-1}) than the rest of the filaments, and which is also spatially correlated

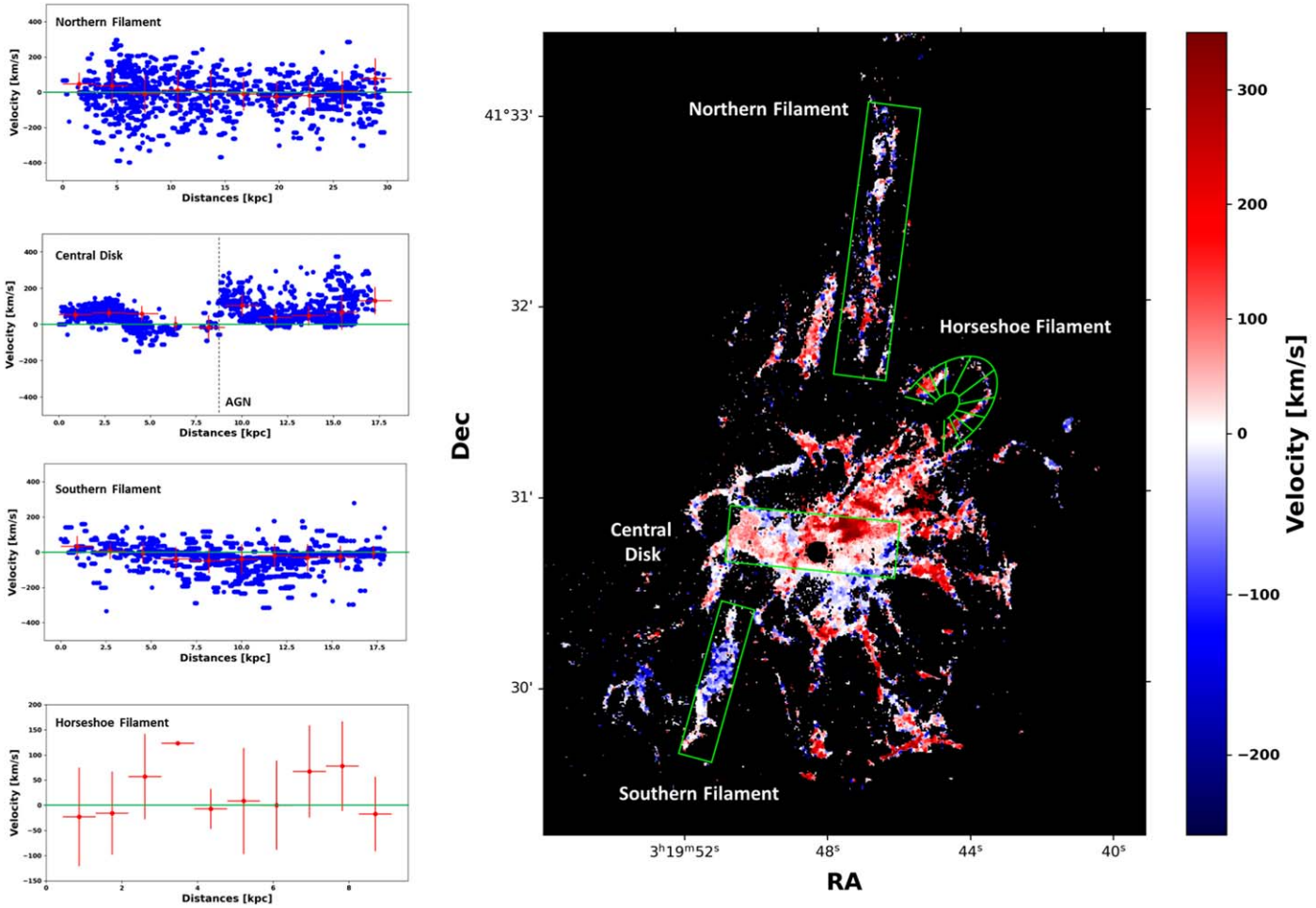

Figure 16. Velocity profiles of selected filaments in the nebula surrounding NGC 1275 (in units of km s^{-1}, where the green lines show zero velocity). For the first three profiles, we show in blue the velocity of each pixel bin found in the region, while the red points illustrates the mean taken in 10 subregions of equal widths. The velocity profile of the Horseshoe filament only displays the mean velocity across 10 subregions.

with a disk-shaped structure as seen in CO(2−1) associated with molecular gas. Both of these structures seem to correlate spatially with the wakes of the radio bubbles that have been inflated through the relativistic jets of the SMBH at the center of the galaxy. However, this disk-shaped feature does not display a clear rotation pattern, which entails a definitive difference from similar structures obtained through simulations.

2. The rest of the filamentary structure displays fainter flux measurement ($\sim 1 \times 10^{-18}$ erg s^{-1} cm^{-2} $Å^{-1}$) as well as a much lower velocity dispersion ($\sim$44 km s^{-1}) across the outer filaments, thus implying a potential more quiescent formation mechanism.
3. Thanks to our very high spectral resolution, we also managed to detect regions and knots displaying multiple emission line components. However, they are extremely localized and only found in the central part of the filamentary nebula within $r < 10$ kpc. Nevertheless, a future study of these structures could potentially help us to gain more insight into the 3D structure of the central filaments.
4. Regarding the formation model explored for this filamentary nebula, it seems that a unified model as explored by Tremblay et al. (2018) could potentially explain the observed characteristics of the flux-emitting gas and velocity dispersion measurements obtained through our analysis of the SITELLE observations of NGC 1275. Indeed, regarding the galaxy-scale fountain model explored by Tremblay et al. (2018) we observe similar trends both in terms of kinematics and velocity dispersion between NGC 1275 and A2597. These similarities are also seen in the comoving nature of filamentary nebulae with both cold molecular structures and surrounding gas. Therefore, a unified model of formation through the inflow of cold molecular clouds toward the AGN could thus feed its accretion and drive the formation of radio bubbles. This would in turn uplift multiphase material away from the BCG which could then precipitate back toward the AGN and supply the fountain, while turbulent radiative mixing layers could form between the hot ICM and cold molecular gas. However, contentious points still remain to be explored to comprehend properly the mechanisms leading to the formation of such extended filamentary nebula.

Through our analysis of new high-spectral-resolution observations of the filamentary nebula surrounding NGC 1275, we reinforced the previous results established by

Gendron-Marsolais et al. (2018) and discovered new structures in the optical emission of the filaments. However, these are the first results obtained with this data set and we expect to get more through an improved analysis of the emission close to the AGN, a study of the SN1 and SN2 filters of SITELLE, as well as the calculation of the velocity structure function with these new maps. Finally, new X-ray observations with the XRISM space telescope (XRISM Science Team 2020), the successor of Hitomi, will enable a breakthrough in the study of AGN feedback. This study will offer a touchstone for the analysis of renewed X-ray observations of NGC 1275.

Acknowledgments

The authors would like to thank the Canada–France–Hawaii Telescope (CFHT) which is operated by the National Research Council (NRC) of Canada, the Institut National des Sciences de l'Univers of the Centre National de la Recherche Scientifique (CNRS) of France, and the University of Hawaii. The observations at the CFHT were performed with care and respect from the summit of Maunakea which is a significant cultural and historic site.

B.V. acknowledges financial support from the physics departement of the Université de Montréal. J. H.-L. acknowledges support from NSERC via the Discovery grant program, as well as the Canada Research Chair program. M.G.-M. acknowledges financial support from the grant CEX2021-001131-S funded by MCIN/AEI/ 10.13039/501100011033, from the coordination of the participation in SKA-SPAIN, funded by the Ministry of Science and Innovation (MCIN). J.L. acknowledges support from the Research Grants Council of Hong Kong through grant 17300620. N.W. is supported by the GACR grant 21-13491X. Y.L. acknowledges financial support from NSF grants AST-2107735 and AST-2219686, NASA grant 80NSSC22K0668, and Chandra X-ray Observatory grant TM3-24005X. L.R.-N. is grateful to the National Science foundation NSF - 2109124 and the Natural Sciences and Engineering Research Council of Canada NSERC - RGPIN-2023-03487 for their support.

B.V. also personally acknowledges Pr. Christopher Conselice for sharing observational data of NGC 1275 in the optical, as well as Dr. Rupal Mittal for sharing Herschel kinematic data of NGC 1275 in the infrared.

Software: python (Van Rossum & Drake 2009), astropy (Robitaille et al. 2013, Price-Whelan et al. 2018), numpy (Harris et al. 2020), scipy (Virtanen et al. 2020), matplotlib (Hunter 2007), and `LUCI` (Rhea et al. 2021a).

Appendix A
Background Variability

In this section, we display two spectra extracted from background regions (see Figure 17), which illustrate the clear variability in background sky emission at high spectral resolution.

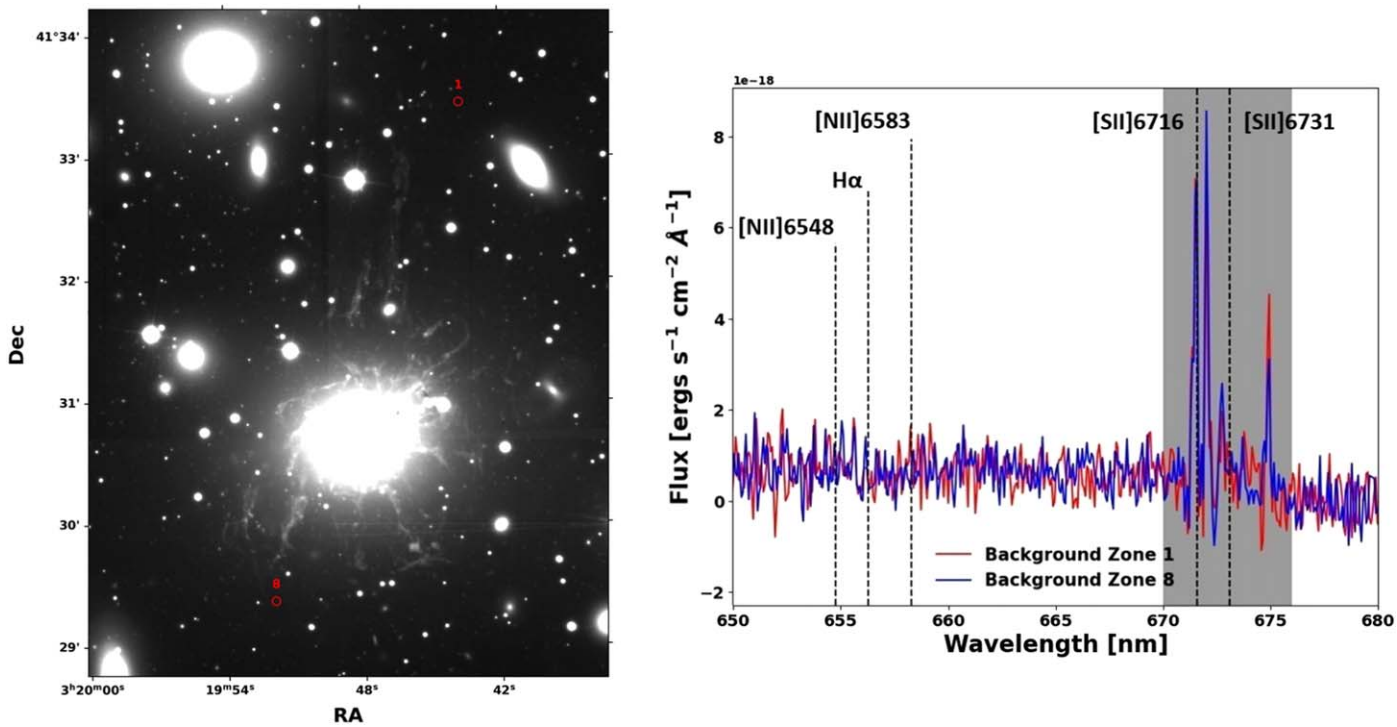

Figure 17. Comparison of the spectra extracted from two background regions denoted by the numbers 1 and 8 at high spectral resolution. The main emission lines positions are indicated by dotted lines. The gray shaded area represents the location of the principal sky lines overlapping with the [S II] emission lines doublet.

Appendix B
S/N Map

In this section, we present an S/N map obtained with the `create_snr_map` function of `LUCI` before applying the WVT binning. As can be seen in Figure 18, the overall S/N is low across the entire filamentary nebula and thus binning is required.

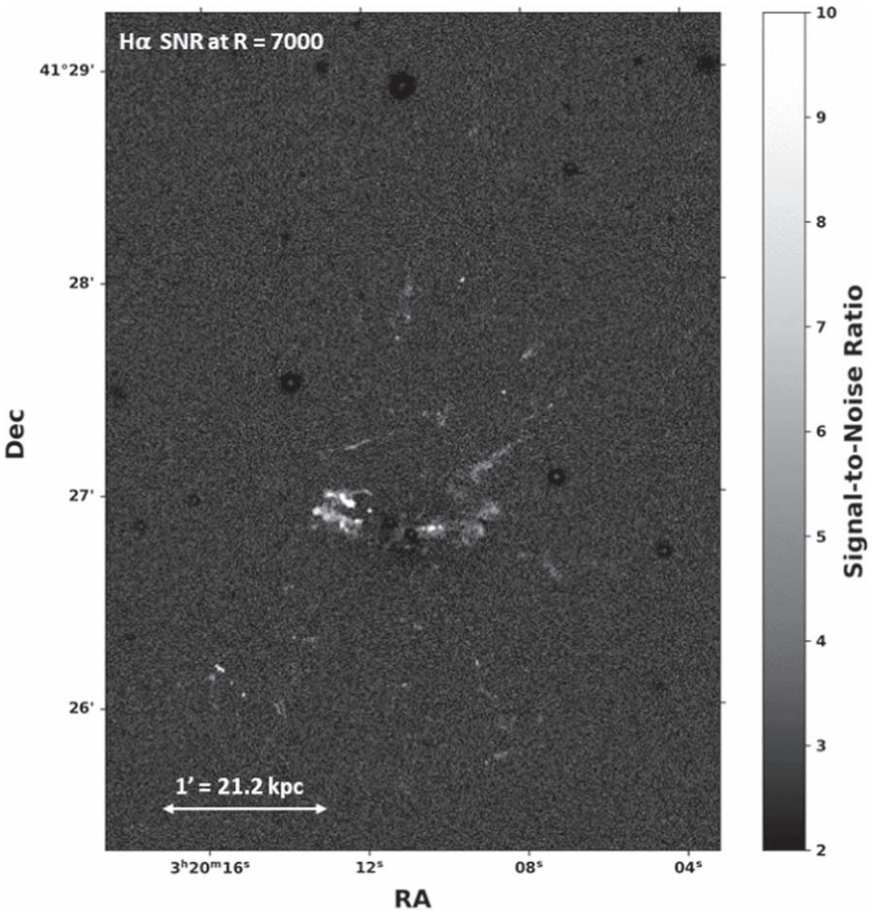

Figure 18. S/N map in linear scale of the high-spectral-resolution SITELLE observations of the filamentary nebula surrounding NGC 1275 .

Appendix C
Multiple Emission Line Components Spectra

In this section, we show a small number of spectra belonging to localized regions of the filamentary nebula and displaying multiple emission line components. Their central respective coordinates are the following: R.A. = 3:19:48.165, decl. = +41:30:54.275; R. A. = 3:19:46.92, decl. = +41:30:51.703; and R.A. = 3:19:46.623, decl. = +41:30:40.277. See Figure 19 below.

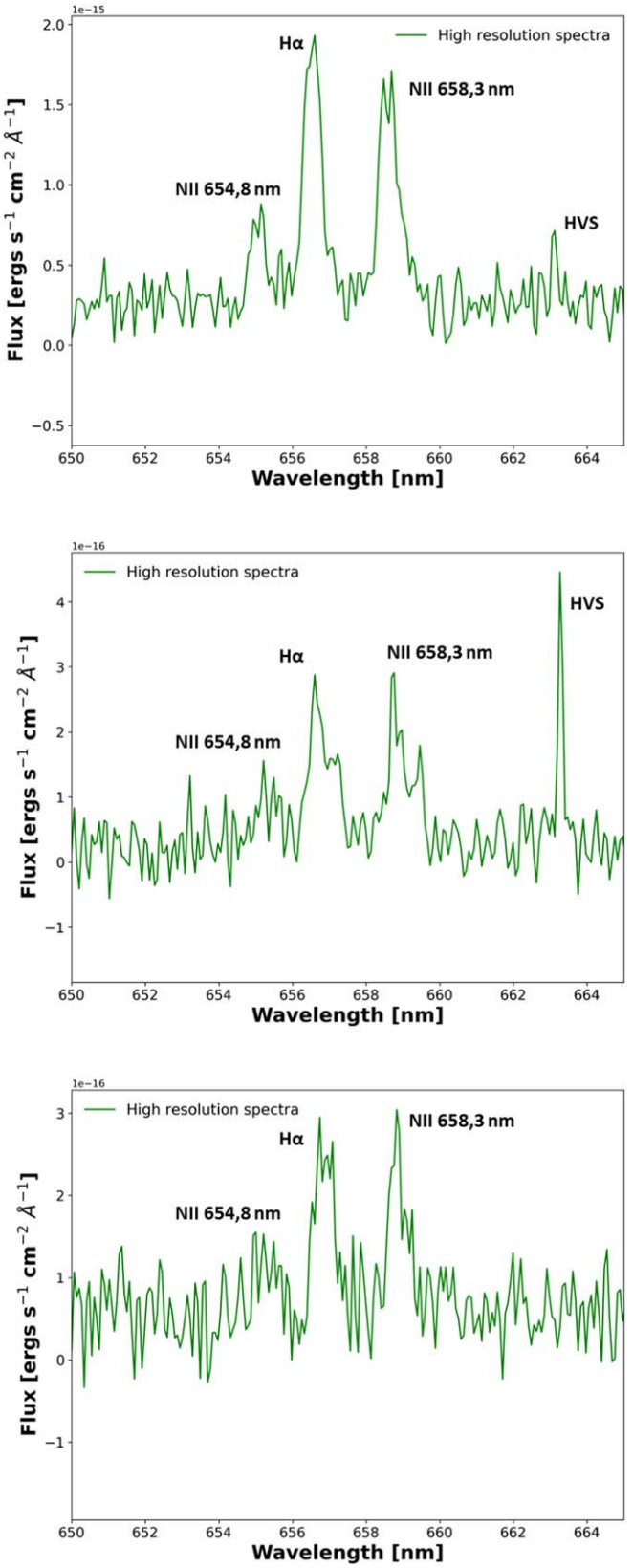

Figure 19. Spectra of localized regions of the filamentary nebula displaying multiple-component emission lines.

ORCID iDs

Benjamin Vigneron https://orcid.org/0000-0002-2478-5119
Julie Hlavacek-Larrondo https://orcid.org/0000-0001-7271-7340
Carter Lee Rhea https://orcid.org/0000-0003-2001-1076
Marie-Lou Gendron-Marsolais https://orcid.org/0000-0002-2478-5119
Jeremy Lim https://orcid.org/0000-0003-4220-2404
Yuan Li https://orcid.org/0000-0001-5262-6150
Laurent Drissen https://orcid.org/0000-0003-1278-2591
Greg L. Bryan https://orcid.org/0000-0003-2630-9228
Megan Donahue https://orcid.org/0000-0002-2808-0853
Alastair Edge https://orcid.org/0000-0002-3398-6916
Andrew Fabian https://orcid.org/0000-0002-9378-4072
Stephen Hamer https://orcid.org/0000-0003-1932-0162
Thomas Martin https://orcid.org/0000-0002-3074-9608
Michael McDonald https://orcid.org/0000-0001-5226-8349
Brian McNamara https://orcid.org/0000-0002-2622-2627
Annabelle Richard-Lafferrière https://orcid.org/0000-0001-7597-270X
Laurie Rousseau-Nepton https://orcid.org/0000-0002-5136-6673
G. Mark Voit https://orcid.org/0000-0002-3514-0383
Tracy Webb https://orcid.org/0000-0002-0104-9653
Norbert Werner https://orcid.org/0000-0003-0392-0120

References

Abell, G. O., Corwin, H. G., Jr, & Olowin, R. P. 1989, ApJS, 70, 1
Abruzzo, M. W., Fielding, D. B., & Bryan, G. L. 2022, arXiv:2210.15679v2
Bahcall, N. A. 1977, ARA&A, 15, 505
Begelman, M. C., & Fabian, A. 1990, MNRAS, 244, 26P
Best, P. N., Von Der Linden, A., Kauffmann, G., Heckman, T. M., & Kaiser, C. R. 2007, MNRAS, 379, 894
Bittner, A., Falcón-Barroso, J., Nedelchev, B., et al. 2019, A&A, 628, A117
Boehringer, H., Voges, W., Fabian, A. C., Edge, A. C., & Neumann, D. M. 1993, MNRAS, 264, L25
Canning, R., Fabian, A., Johnstone, R., et al. 2010, MNRAS, 405, 115
Canning, R. E. A., Ryon, J. E., Gallagher, J. S., et al. 2014, MNRAS, 444, 336
Cavaliere, A. G., Gursky, H., & Tucker, W. H. 1971, Natur, 231, 437
Conselice, C. J., Gallagher, J. S., III, & Wyse, R. F. 2001, AJ, 122, 2281
Crawford, C. S., Allen, S. W., Ebeling, H., Edge, A. C., & Fabian, A. C. 1999, MNRAS, 306, 857
Dhawan, V., Kellermann, K. I., & Romney, J. D. 1998, ApJL, 498, L111
Drissen, L., Martin, T., Rousseau-Nepton, L., et al. 2019, MNRAS, 485, 3930
Dutta, A., Sharma, P., & Nelson, D. 2022, MNRAS, 510, 3561
Fabian, A., Ferland, G., Sanders, J., et al. 2022, MNRAS, 515, 3336
Fabian, A., Sanders, J., Ferland, G., et al. 2023a, MNRAS, 521, 1794
Fabian, A., Sanders, J., Ferland, G., et al. 2023b, MNRAS, 524, 716
Fabian, A., Tawara, Y., Bautz, M., & Arnaud, K. 1994, ApJL, 436, 63
Fabian, A. C., Johnstone, R. M., Sanders, J. S., et al. 2008, Natur, 454, 968
Fabian, A. C., Sanders, J. S., Allen, S. W., et al. 2011, MNRAS, 418, 2154
Fabian, A. C., Sanders, J. S., Crawford, C. S., et al. 2003, MNRAS, 344, L48
Fabian, A. C., Sanders, J. S., Ettori, S., et al. 2000, MNRAS, 318, L65
Fabian, A. C., Walker, S., Russell, H., et al. 2016a, MNRAS, 461, 922
Fabian, A. C., Walker, S. A., Russell, H. R., et al. 2016b, MNRAS, 461, 922
Falceta-Gonçalves, D., de Gouveia Dal Pino, E. M., Gallagher, J. S., & Lazarian, A. 2010, ApJL, 708, L57
Ferland, G. J., Fabian, A. C., Hatch, N. A., et al. 2009, MNRAS, 392, 1475
Fielding, D. B., & Bryan, G. L. 2022, ApJ, 924, 82
Forman, W., Kellogg, E., Gursky, H., Tananbaum, H., & Giacconi, R. 1972, ApJ, 178, 309
Gaia Collaboration 2020, yCat, I/350
Gaspari, M., Brighenti, F., & Temi, P. 2015, A&A, 579, A62
Gaspari, M., Ruszkowski, M., & Oh, S. P. 2013, MNRAS, 432, 3401
Gaspari, M., Ruszkowski, M., & Sharma, P. 2012, ApJ, 746, 94
Gendron-Marsolais, M., Hlavacek-Larrondo, J., Martin, T. B., et al. 2018, MNRAS, 479, L28
Gendron-Marsolais, M., Hlavacek-Larrondo, J., van Weeren, R. J., et al. 2020, MNRAS, 499, 5791
Graham, J., Fabian, A. C., & Sanders, J. S. 2008, MNRAS, 386, 278
Gursky, H., Kellogg, E. M., Leong, C., Tananbaum, H., & Giacconi, R. 1971, ApJL, 165, L43
Hamer, S. L., Edge, A. C., Swinbank, A. M., et al. 2014, MNRAS, 437, 862
Hamer, S. L., Edge, A. C., Swinbank, A. M., et al. 2016, MNRAS, 460, 1758

Harris, C. R., Millman, K. J., van der Walt, S. J., et al. 2020, Natur, 585, 357
Hatch, N. A., Crawford, C. S., Johnstone, R. M., & Fabian, A. C. 2006, MNRAS, 367, 433
Hitomi Collaboration, Aharonian, F., Akamatsu, H., et al. 2016, Natur, 535, 117
Hitomi Collaboration, Aharonian, F., & Akamatsu, H. 2018, PASJ, 70, 9
Ho, I. T., Lim, J., & Dinh-V-Trung 2009, ApJ, 698, 1191
Hudson, D. S., Mittal, R., Reiprich, T. H., et al. 2010, A&A, 513, A37
Hunter, J. D. 2007, CSE, 9, 90
Ji, S., Oh, S. P., & Masterson, P. 2019, MNRAS, 487, 737
Johnstone, R., Fabian, A., Edge, A., & Thomas, P. 1992, MNRAS, 255, 431
Kent, S. M., & Sargent, W. L. W. 1979, ApJ, 230, 667
Kewley, L. J., Groves, B., Kauffmann, G., & Heckman, T. 2006, MNRAS, 372, 961
Kewley, L. J., Nicholls, D. C., & Sutherland, R. S. 2019, ARA&A, 57, 511
Li, Y., & Bryan, G. L. 2014a, ApJ, 789, 153
Li, Y., & Bryan, G. L. 2014b, ApJ, 789, 54
Li, Y., Bryan, G. L., Ruszkowski, M., et al. 2015, ApJ, 811, 73
Lim, J., Ao, Y., & Dinh-V-Trung 2008, ApJ, 672, 252
Lim, J., Ohyama, Y., Yan, C.-H., Dinh-V-Trung, & Wang, S.-Y. 2012, ApJ, 744, 112
Lynds, R. 1970, ApJL, 159, L151
Martin, T. B., Prunet, S., & Drissen, L. 2016, MNRAS, 463, 4223
McDonald, M., Veilleux, S., Rupke, D. S. N., & Mushotzky, R. 2010, ApJ, 721, 1262
McNamara, B. R., & Nulsen, P. E. J. 2007, ARA&A, 45, 117
McNamara, B. R., O'Connell, R. W., & Sarazin, C. L. 1996, AJ, 112, 91
McNamara, B. R., Russell, H. R., Nulsen, P. E. J., et al. 2014, ApJ, 785, 44
McNamara, B. R., Russell, H. R., Nulsen, P. E. J., et al. 2016, ApJ, 830, 79
Million, E., & Allen, S. 2009, MNRAS, 399, 1307
Minkowski, R. 1957, in IAU Symp. 4, Radio Astronomy, ed. E. C. van de Hulst (Cambridge: Cambridge Univ. Press), 107
Mittal, R., Oonk, J. R., Ferland, G. J., et al. 2012, MNRAS, 426, 2957
Nagai, H., Onishi, K., Kawakatu, N., et al. 2019, ApJ, 883, 193
Price-Whelan, A. A. M., Sipőcz, B. M., Günther, H. M., et al. 2018, AJ, 156, 123
Randall, S. W., Nulsen, P. E. J., Jones, C., et al. 2015, ApJ, 805, 112
Rhea, C., Hlavacek-Larrondo, J., Perreault-Levasseur, L., Gendron-Marsolais, M.-L., & Kraft, R. 2020a, AJ, 160, 202
Rhea, C., Hlavacek-Larrondo, J., Rousseau-Nepton, L., Vigneron, B., & Guité, L.-S. 2021a, RNAAS, 5, 208
Rhea, C., Rousseau-Nepton, L., Prunet, S., et al. 2021b, ApJ, 910, 129
Rhea, C., Rousseau-Nepton, L., Prunet, S., Hlavacek-Larrondo, J., & Fabbro, S. 2020b, ApJ, 901, 152
Riffel, R. A., Storchi-Bergmann, T., Zakamska, N. L., & Riffel, R. 2020, MNRAS, 496, 4857
Robitaille, T. P., Tollerud, E. J., Greenfield, P., et al. 2013, A&A, 558, A33
Rousseau-Nepton, L., Martin, R. P., Robert, C., et al. 2019, MNRAS, 489, 5530
Rubin, V., Oort, J., Ford, W., & Peterson, C. 1977, ApJ, 211, 693
Russell, H. R., McNamara, B. R., Fabian, A. C., et al. 2019, MNRAS, 490, 3025
Salomé, P., Combes, F., Edge, A. C., et al. 2006, A&A, 454, 437
Salomé, P., Combes, F., Revaz, Y., et al. 2008, A&A, 484, 317
Salomé, P., Combes, F., Revaz, Y., et al. 2011, A&A, 531, A85
Sanchez Almeida, J., Terlevich, R., Terlevich, E., Fernandes, R., & Morales-Luis, A. 2012, ApJ, 756, 163
Sand, D. J., Treu, T., Smith, G. P., & Ellis, R. S. 2004, ApJ, 604, 88
Tremblay, G. R., Combes, F., Oonk, J. B. R., et al. 2018, ApJ, 865, 13
Van Rossum, G., & Drake, F. L. 2009, The Python Language Reference, Vol. 561 (Amsterdam: Python Software Foundation)
Virtanen, P., Gommers, R., Oliphant, T. E., et al. 2020, NatMe, 17, 261
Voigt, L. M., & Fabian, A. C. 2006, MNRAS, 368, 518
Voit, G., Donahue, M., Bryan, G., & McDonald, M. 2015, Natur, 519, 203
Voit, G. M. 2018, ApJ, 868, 102
Voit, G. M., Cavagnolo, K. W., Donahue, M., et al. 2008, ApJL, 681, L5
Voit, G. M., & Donahue, M. 2015, ApJL, 799, L1
Voit, G. M., Meece, G., Li, Y., et al. 2017, ApJ, 845, 80
Walker, S. A., Kosec, P., Fabian, A. C., & Sanders, J. S. 2015, MNRAS, 453, 2480
White, D., Fabian, A., Johnstone, R., Mushotzky, R., & Arnaud, K. 1991, MNRAS, 252, 72
XRISM Science Team 2020, arXiv:2003.04962
Yang, H.-Y. K., Gaspari, M., & Marlow, C. 2019, ApJ, 871, 6
Yu, A. P. Y., Lim, J., Ohyama, Y., Chan, J. C. C., & Broadhurst, T. 2015, ApJ, 814, 101
Zeidler, P., Nota, A., Sabbi, E., et al. 2019, AJ, 158, 201
Zhang, C., Zhuravleva, I., Gendron-Marsolais, M.-L., et al. 2022, MNRAS, 517, 616
Zhuravleva, I., Churazov, E., Schekochihin, A. A., et al. 2014, Natur, 515, 85